



# Structural Parameters and Possible Association of the Ultra-faint Dwarfs Pegasus III and Pisces II from Deep Hubble Space Telescope Photometry

Hannah Richstein<sup>1</sup>, Ekta Patel<sup>2,3</sup>, Nitya Kallivayalil<sup>1</sup>, Joshua D. Simon<sup>4</sup>, Paul Zivick<sup>5</sup>, Erik Tollerud<sup>6</sup>, Tobias Fritz<sup>1</sup>, Jack T. Warfield<sup>1</sup>, Gurtina Besla<sup>7</sup>, Roeland P. van der Marel<sup>6,8</sup>, Andrew Wetzel<sup>9</sup>, Yumi Choi<sup>2,6</sup>, Alis Deason<sup>10,11</sup>, Marla Geha<sup>12</sup>, Puragra Guhathakurta<sup>13</sup>, Myoungwon Jeon<sup>14</sup>, Evan N. Kirby<sup>15,16</sup>, Mattia Libralato<sup>17</sup>, Elena Sacchi<sup>18,19</sup>, and Sangmo Tony Sohn<sup>6</sup>

<sup>1</sup> University of Virginia, Department of Astronomy, 530 McCormick Road, Charlottesville, VA 22904, USA; [hr8jz@virginia.edu](mailto:hr8jz@virginia.edu)

<sup>2</sup> Department of Astronomy, University of California Berkeley, 501 Campbell Hall, Berkeley, CA 94720, USA

<sup>3</sup> Miller Institute for Basic Research in Science, 468 Donner Lab, Berkeley, CA 94720, USA

<sup>4</sup> Observatories of the Carnegie Institution for Science, 813 Santa Barbara Street, Pasadena, CA 91101, USA

<sup>5</sup> Mitchell Institute for Fundamental Physics and Astronomy, Department of Physics and Astronomy, Texas A & M University, 578 University Drive, College Station, TX 77843, USA

<sup>6</sup> Space Telescope Science Institute, 3700 San Martin Drive, Baltimore, MD 21218, USA

<sup>7</sup> Steward Observatory, University of Arizona, 933 North Cherry Avenue, Tucson, AZ 85721, USA

<sup>8</sup> Center for Astrophysical Sciences, The William H. Miller III Department of Physics & Astronomy, Johns Hopkins University, 3400 North Charles Street, Baltimore, MD 21218, USA

<sup>9</sup> Department of Physics & Astronomy, University of California Davis, One Shields Avenue, Davis, CA 95616, USA

<sup>10</sup> Institute for Computational Cosmology, Department of Physics, University of Durham, South Road, Durham DH1 3LE, UK

<sup>11</sup> Centre for Extragalactic Astronomy, Department of Physics, University of Durham, South Road, Durham DH1 3LE, UK

<sup>12</sup> Department of Astronomy, Yale University, 52 Hillhouse Avenue, New Haven, CT 06520, USA

<sup>13</sup> UCO/Lick Observatory, Department of Astronomy & Astrophysics, University of California Santa Cruz, 1156 High Street, Santa Cruz, CA 95064, USA

<sup>14</sup> Department of Astronomy & Space Science, Kyung Hee University, 1732 Deogyong-daero, Yongin-si, Gyeonggi-do 17104, Republic of Korea

<sup>15</sup> Department of Astronomy, California Institute of Technology, 1200 East California Boulevard, MC 249-17, Pasadena, CA 91125, USA

<sup>16</sup> Department of Physics, University of Notre Dame, 225 Nieuwland Science Hall, Notre Dame, IN 46556, USA

<sup>17</sup> AURA for the European Space Agency (ESA), Space Telescope Science Institute, 3700 San Martin Drive, Baltimore, MD 21218, USA

<sup>18</sup> Leibniz-Institut für Astrophysik Potsdam, An der Sternwarte 16, D-14482 Potsdam, Germany

<sup>19</sup> INAF-Osservatorio di Astrofisica e Scienza dello Spazio di Bologna, Via Gobetti 93/3, I-40129 Bologna, Italy

Received 2022 April 4; revised 2022 May 9; accepted 2022 May 19; published 2022 July 15

## Abstract

We present deep Hubble Space Telescope (HST) photometry of the ultra-faint dwarf (UFD) galaxies Pegasus III (Peg III) and Pisces II (Psc II), two of the most distant satellites in the halo of the Milky Way (MW). We measure the structure of both galaxies, derive mass-to-light ratios with newly determined absolute magnitudes, and compare our findings to expectations from UFD-mass simulations. For Peg III, we find an elliptical half-light radius of  $a_h = 1.88^{+0.42}_{-0.33}$  ( $118^{+31}_{-30}$  pc) and  $M_V = -4.17^{+0.19}_{-0.22}$ ; for Psc II, we measure  $a_h = 1.31^{+0.10}_{-0.09}$  ( $69 \pm 8$  pc) and  $M_V = -4.28^{+0.19}_{-0.16}$ . We do not find any morphological features that indicate a significant interaction between the two has occurred, despite their close separation of only  $\sim 40$  kpc. Using proper motions (PMs) from Gaia early Data Release 3, we investigate the possibility of any past association by integrating orbits for the two UFDs in an MW-only and a combined MW and Large Magellanic Cloud (LMC) potential. We find that including the gravitational influence of the LMC is crucial, even for these outer-halo satellites, and that a possible orbital history exists where Peg III and Psc II experienced a close ( $\sim 10$ – $20$  kpc) passage about each other just over  $\sim 1$  Gyr ago, followed by a collective passage around the LMC ( $\sim 30$ – $60$  kpc) just under  $\sim 1$  Gyr ago. Considering the large uncertainties on the PMs and the restrictive priors imposed to derive them, improved PM measurements for Peg III and Psc II will be necessary to clarify their relationship. This would add to the rare findings of confirmed pairs of satellites within the Local Group.

*Unified Astronomy Thesaurus concepts:* Dwarf galaxies (416); Local Group (929); Galaxy structure (622)

## 1. Introduction

Ultra-faint dwarf (UFD) galaxies are the most dark-matter-dominated systems discovered, and thus a preferred laboratory for studying how well cosmological models predict behavior on small scales. The widely accepted Lambda cold dark matter ( $\Lambda$ CDM) model uses the hierarchical accretion of low-mass systems to explain the growth of dark-matter halos (e.g., Navarro et al. 1997). As UFDs occupy the least-massive

dark-matter halos discovered, they could be considered remnants of this hierarchical process while themselves having formed prior to the epoch of reionization and undergoing little evolution since then (e.g., Ricotti & Gnedin 2005; Gnedin & Kravtsov 2006; Bovill & Ricotti 2009).

The dark-matter halos in which UFDs reside have extrapolated virial masses of approximately  $10^9 M_\odot$  (e.g., Strigari et al. 2008), about two orders of magnitude smaller than where the  $\Lambda$ CDM theory predicts central dark-matter densities in apparent contrast with observations. Dark-matter-only simulations predict cusps, while observations of dwarf spiral and dwarf spheroidal galaxies (dSphs) show cored mass distributions (e.g., Flores & Primack 1994; Moore 1994; Read & Gilmore 2005; Goerdt et al. 2006). Other analyses have

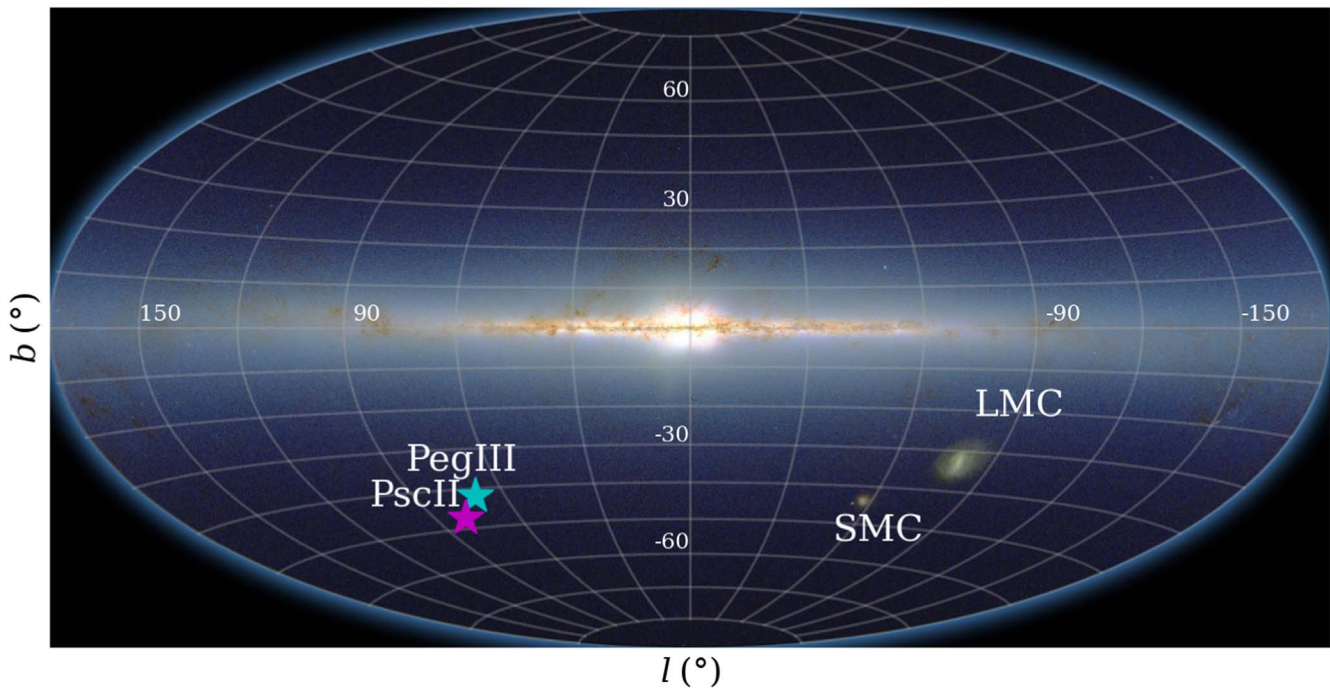


**Figure 1.** Peg III (cyan star) and Psc II (magenta star) shown relative to the Galactic plane, LMC, and SMC. Atlas image mosaic obtained as part of the Two Micron All Sky Survey, a joint project of the University of Massachusetts and the Infrared Processing and Analysis Center/California Institute of Technology, funded by the National Aeronautics and Space Administration and the National Science Foundation (Skrutskie et al. 2006).

suggested that dSphs are consistent with the expected dark-matter density profiles (e.g., Breddels & Helmi 2013; Jarrel & Gebhardt 2013; Strigari et al. 2017; Read et al. 2018, 2019).

A limiting factor for observational constraints is that we are often restricted to line-of-sight (LOS) velocity data of the stars residing in dwarf galaxies, and with no information on the tangential velocity components, we suffer from the mass-anisotropy degeneracy. It will thus take more information, such as the shape of the velocity distribution or galactic internal proper motions (PMs), in addition to radial velocities to be able to distinguish a dark-matter central core or cusp (e.g., Strigari et al. 2007; Guerra et al. 2021; Read et al. 2021). Once we have full kinematic information, current virial mass estimators can be extended to further constrain UFD dark-matter halo properties (Errani et al. 2018). In the meantime, we can use more easily measured UFD properties such as half-light radius and luminosity to explore the population as a whole, as well as their simulated analogs.

Defined by having  $M_V$  values fainter than  $-7.7$  (e.g., Bullock & Boylan-Kolchin 2017; Simon 2019), UFDs went undetected until the advent of large-scale digital sky surveys, beginning with the Sloan Digital Sky Survey (SDSS) in 2005 (York et al. 2000; Willman et al. 2005). Currently, over 21 UFDs have been spectroscopically verified, and more than 20 other candidates have been identified (e.g., Simon 2019). These numbers are expected to increase further with the beginning of data collection at the Vera C. Rubin Observatory.

While there is much to learn from studying any of these faint satellites, examining the relatively isolated UFDs at larger Galactocentric distances is particularly useful, as they are more comparable to those produced in most simulations that resolve down to the UFD mass level ( $M_{\text{vir}} \simeq 10^9 M_\odot$  at  $z=0$ ) (e.g., Jeon et al. 2017, 2021a, 2021b; Wheeler et al. 2019). More recently, Applebaum et al. (2021) and Grand et al. (2021) were also able to resolve down to UFD mass scale using

cosmological Milky Way (MW) zoom-in simulations. Comparing the properties of observed UFDs to both of these types of simulations could help us to disentangle the effects that host galaxies may have on their satellite UFDs.

Pegasus III (Peg III) is located at a heliocentric distance of approximately 215 kpc ( $R_{\text{GC}} \sim 213$  kpc; Kim et al. 2016) and is thus one of the most distant MW UFDs known. Peg III was reported in Kim et al. (2015), having been discovered in Data Release 10 of SDSS (Ahn et al. 2014) and confirmed with the Dark Energy Camera. The discovery team noted the proximity ( $\sim 30$  kpc projected and  $\sim 32$  kpc LOS separation) of Peg III to Pisces II (Psc II;  $R_\odot \sim 183$  kpc,  $R_{\text{GC}} \sim 182$  kpc; Belokurov et al. 2010; Sand et al. 2012) at the time and suggested the possibility of an association. Figure 1 shows where Peg III and Psc II lie in relation to the Galactic plane, as well as the LMC and the Small Magellanic Cloud (SMC; Skrutskie et al. 2006). In a follow-up paper using Magellan/IMACS for photometry and Keck/DEIMOS for spectroscopy, Kim et al. (2016) derived a radial velocity for Peg III that, in the Galactic standard-of-rest, only differed from that of Psc II by  $\sim 10 \text{ km s}^{-1}$  ( $-67.6 \pm 2.6$  and  $-79.9 \pm 2.7 \text{ km s}^{-1}$  (Kirby et al. 2015), respectively), and calculated a 3D separation of  $\sim 43$  kpc. Their team also found Peg III to have an irregular shape elongated in the direction of Psc II.

More recently, Garofalo et al. (2021) used the Large Binocular Telescope (LBT) to study variable stars in both UFDs. Using isodensity contour maps, they found no support for a physical connection between Peg III and Psc II, as neither UFD appeared to have an irregular shape. They suggested that the regular structures of both UFDs eliminate the notion of a stellar stream or another clear link between them. However, even if the two UFDs themselves have not interacted, the possibility of them infalling as a pair or as part of a group is not precluded (e.g., Wetzel et al. 2015).

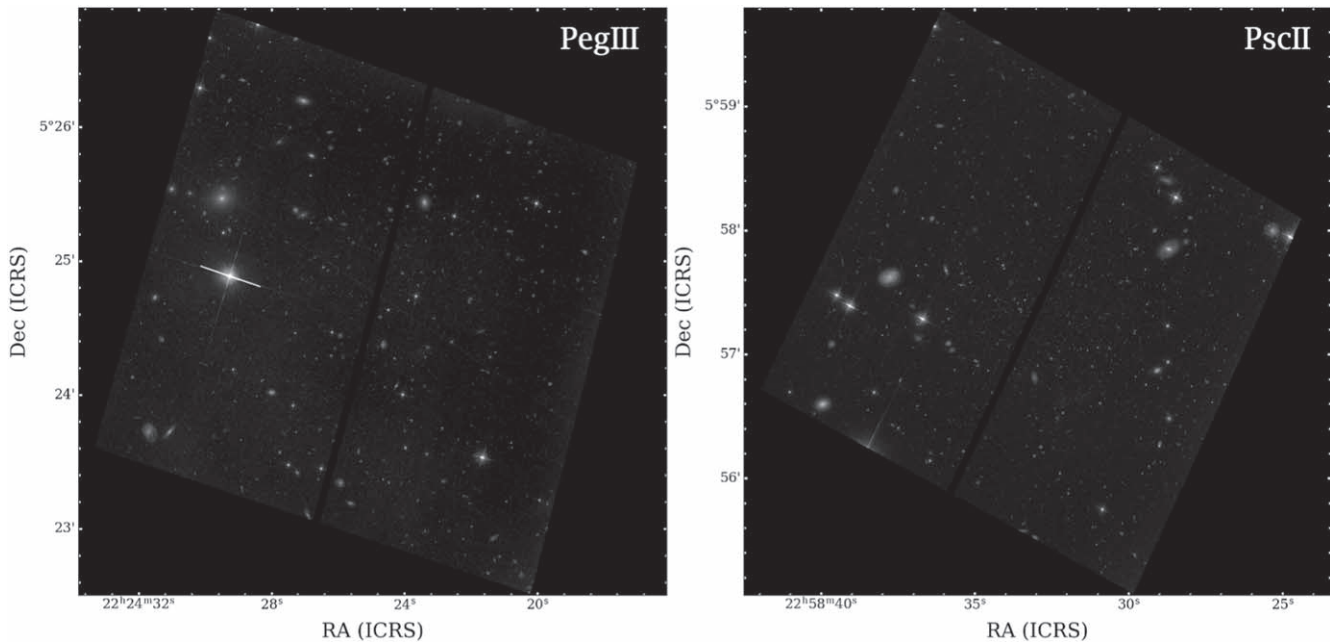


**Figure 2.** False-color images of the ACS fields for Peg III (left) and Psc II (right). The F606W image is used for the blue channel, the F814W for the red channel, and an average of the two for the green channel (Robitaille & Bressert 2012). At the distance of Peg III (215 kpc; Kim et al. 2016),  $1'$  corresponds to  $\sim 63$  pc. For Psc II at 183 kpc (Sand et al. 2012),  $1'$  corresponds to  $\sim 53$  pc.

Here, we present new, deep Hubble Space Telescope (HST) imaging of Peg III and Psc II, allowing further exploration of how these two UFDs may or may not be associated. We produce photometric catalogs and derive structural parameters, integrated  $V$ -band magnitudes, and mass-to-light ratios. We also conduct an orbital analysis of the two UFDs using PMs from Gaia (Gaia Collaboration et al. 2016) early Data Release 3 (eDR3; Gaia Collaboration et al. 2021). In Section 2, we present our data and describe how they were processed. We measure the structural parameters and calculate mass-to-light ratios in Section 3. In Section 4, we use Gaia eDR3 to examine whether Peg III and Psc II could have had a past interaction. We discuss our results and conclude in Sections 5 and 6, respectively.

## 2. Hubble Space Telescope Data

### 2.1. Observations

The observations of Peg III and Psc II were performed using the F606W and F814W filters of the HST Advanced Camera for Surveys (ACS) Wide Field Channel as part of Treasury program GO-14734 (PI: N. Kallivayalil). Parallel, off-target fields were simultaneously taken with the Wide Field Camera 3 (WFC3) using the same filters on the UV/visible channel for the purpose of learning more about the UFD stars farther from their galactic centers (when applicable) and being able to better characterize the stellar background distributions. The Peg III observations were taken on 2017 April 26 and 2017 May 2 using two orbits for F606W and two orbits for F814W. Psc II was observed between 2017 June 19 and 2017 July 12 with two orbits dedicated to each filter. Each pair of ACS exposures totaled 4744 s, while each WFC3 pair totaled 5117 s. The long integration times allowed us to reach a signal-to-noise ratio of 250 at  $m_{F606W} = 23$ . The observations for both galaxies covered a single ACS  $202'' \times 202''$  field and a single WFC3  $162'' \times 162''$  off-field. The visits for each UFD were performed

within a restricted orientation range and over a four-point dither pattern, optimized for the astrometric goals of this Treasury program, but suitable for photometry as well.

### 2.2. Reduction and Photometry

The images were processed and corrected for charge transfer inefficiency using the current ACS and WFC3 pipelines. In each filter, the four dithered images were combined using the DRIZZLE package (Fruchter & Hook 2002) to create `drc` fits files. False-color images (Robitaille & Bressert 2012) of the two drizzled fields are shown in Figure 2. Jackknife resampling was performed on the separate dither images to create four three-dither-combined images for deriving empirical errors. We used the `photutils` (Bradley et al. 2020) routines `DAOSTarFinder` and `aperture_photometry` to detect sources and calculate the flux inside two sizes of circular apertures. After analyzing flux counts from different apertures, we found that a four-pixel radius was both large enough to capture the concentrated stellar light and small enough to avoid the inclusion of light from neighboring sources. By extending the aperture radius by two pixels to create a six-pixel radius, we could determine whether a source was more extended and thus not a star.

We used the four- and six-pixel instrumental magnitudes ( $m_{\text{inst}}$ ) to create a flag differentiating stars from galaxies. First, we calculated the median magnitude difference between the four- and six-pixel radius values and then determined the uncertainty of the difference between the four- and six-pixel binned  $m_{\text{inst}}$  values as a function of the four-pixel  $m_{\text{inst}}$ . After accounting for an error floor, we fit a linear relation to these uncertainties as a function of flux. We considered a source to be a star if its magnitude difference from the median was within  $2\sigma$  of the fitted functional value. This criterion excluded galaxies, which showed larger magnitude differences as well as deviation from the fitted relation between the four- and six-pixel  $m_{\text{inst}}$ . After applying the flags, we accounted for the



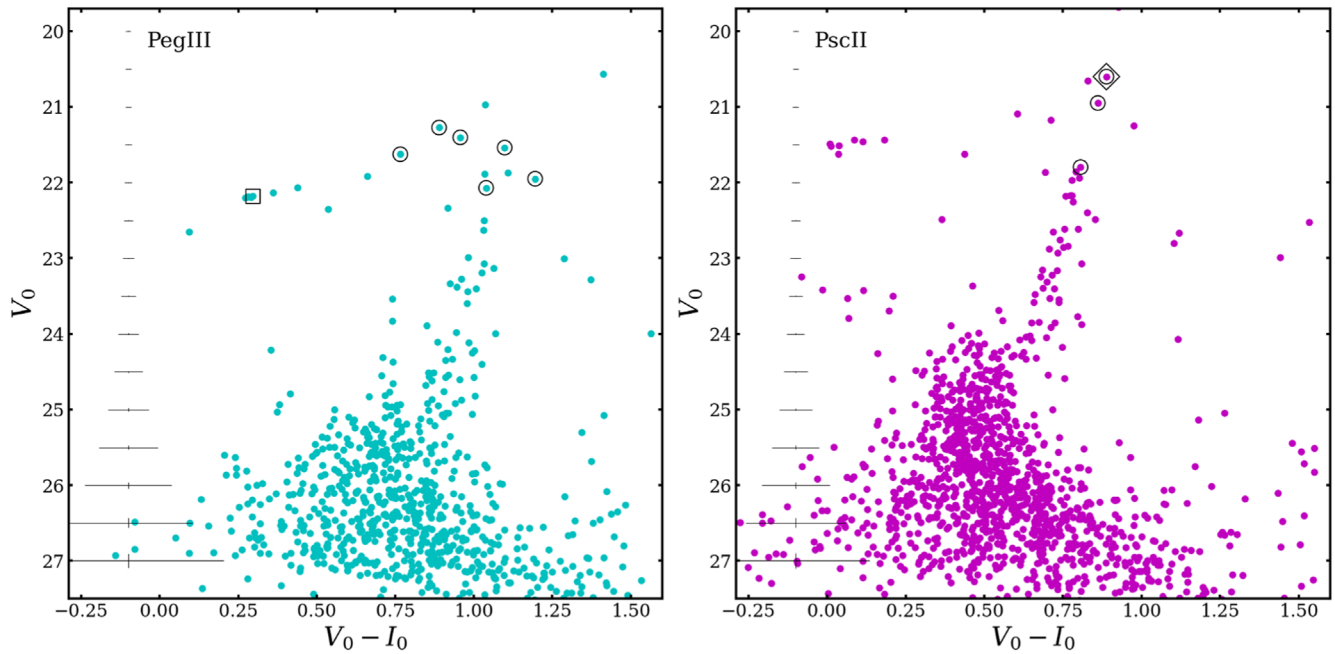


**Figure 3.** CMDs of Peg III (left) and Psc II (right) in VEGAMAG. The typical color and magnitude errors are shown to the left. Confirmed spectroscopic members in our catalog are shown in circles for Peg III, along with a star that has ambiguous membership in a square (Kim et al. 2016). There is one Peg III spectroscopic member that is not included in our catalog due to it falling within the ACS chip gap. The Psc II spectroscopic members with matches in our catalog are shown in circles (Kirby et al. 2015). Only three of the seven member stars fall within the ACS field-of-view (FOV). The spectroscopic member with a Gaia PM is in the diamond. The other stars used in the Psc II PM measurement were either too bright or not in the ACS FOV. Only sources flagged as stars are shown.

encircled energy corrections on the four-pixel radius flux values, converted the flux to STMAG, and matched sources between the F606W and F814W images. If a source was flagged as a star in either filter, it was used in the analysis for this paper.

Sources in the three-dither combined images went through the same aperture photometry pipeline and were matched across the four combinations in each filter using a six-parameter linear transformation. To derive empirical errors, we took the standard deviation of the magnitudes of the sources found across all of the combined images. The sources were matched in the F606W and F814W filters, then matched to the `drc` source list using the same six-parameter transformation.

The observed magnitudes were corrected for dust extinction and reddening using the `dustmaps` module (Green 2018) with the Schlegel et al. (1998) maps and Schlafly & Finkbeiner (2011) recalibration. We converted the ACS photometry from STMAG filters to VEGAMAG  $V$  and  $I$  using the conversions and zero-points given in Sirianni et al. (2005). To convert the WFC3 photometry, we employed `synphot` (STScI Development Team 2018) to generate representative blackbodies of field stars (5200 and 5100 K for the Peg III and Psc II off-fields). Finally, we used `stsynphot` (STScI Development Team 2010) to calculate the filter conversion terms for these blackbodies and the WFC3 VEGAMAG zero-points for the observation dates. The resulting color–magnitude diagrams (CMDs) and typical errors are shown in Figure 3, where cuts have been made based on the *star-galaxy* flag.

To present the data and to explore the existence of the elongation in Peg III measured by Kim et al. (2016), we created a contour map of stellar number density by performing a kernel density estimate on the data using  $67\ 4''.5 \times 4''.5$  bins. The maps are oriented such that north is in the direction of the positive  $y$ -axis and east is in the direction of the negative  $x$ -axis.

The left panel of Figure 4 shows the 10 levels as filled contours for Peg III. There is an overdensity in the northwest (NW); however, it is not in the direction of Psc II, which is indicated by the white arrow pointing from the center to the east. The contour map for Psc II is illustrated in the right panel of Figure 4, created using the same process as for the Peg III map. This is consistent with density contour maps from Belokurov et al. (2010), Sand et al. (2012), Muñoz et al. (2018), and Garofalo et al. (2021), as all show Psc II with more regular levels. Comparing Psc II to Peg III, we see that Psc II is more compact and has a higher peak smoothed surface density.

### 3. Structural Analysis

#### 3.1. Fitting 2D Profiles

To model the spatial structures of Peg III and Psc II, we followed the technique described in Drlica-Wagner et al. (2020) and Simon et al. (2021), largely based on the method shown in Martin et al. (2008). We modeled each UFD with exponential and Plummer (Plummer 1911) profiles and performed binned Poisson maximum likelihood fits to the probability density functions with the following free parameters: center position ( $x_0, y_0$ ), richness (number of stars), 2D, projected semimajor axis of the ellipse that contains half of the total integrated surface density of the galaxy (elliptical half-light radius;  $a_h$ ), ellipticity ( $\epsilon$ ), position angle of the semimajor axis measured East through North ( $\theta$ ), and background surface density (average density of stars in the field not belonging to the galaxy) ( $\Sigma_b$ ). In past literature on these UFDs, the elliptical half-light radius  $a_h$  has often been referred to as  $r_h$ , but here we have chosen to make the explicit distinction between  $a_h$  and the azimuthally averaged half-light radius  $r_h$  (equal to  $a_h\sqrt{1-\epsilon}$ ) for clarity and the purpose of our comparison to simulations.

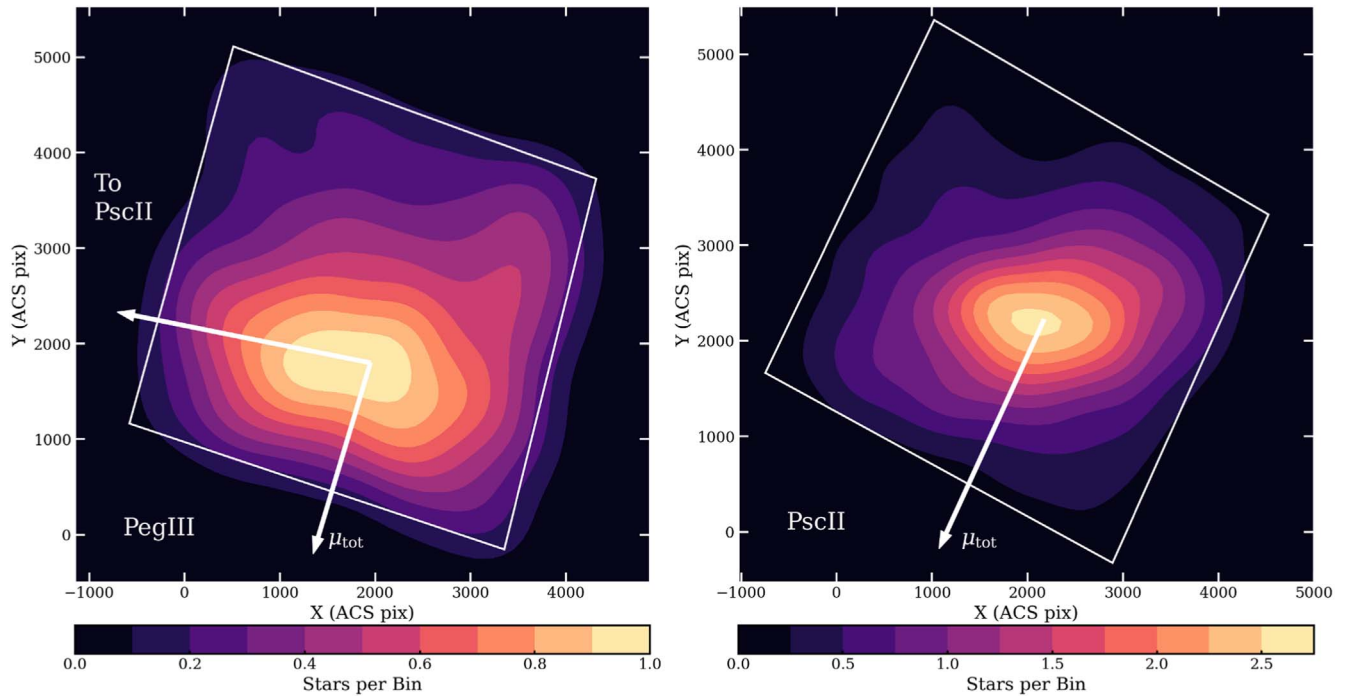


**Figure 4.** Density contour maps of Peg III (left) and Psc II (right). Each map shows 10 levels defined by the color bar and in units of stars per  $4''.5 \times 4''.5$  bin. Note that the two color bars have different ranges and are not integer values as they are from kernel density estimates. The white lines show the borders of the ACS FOV, and the white arrows represent  $\mu_{\text{tot}}$  over a timespan of 0.5 Myr from McConnell & Venn (2020). In this and all subsequent plots, the galaxies are oriented such that north is in the direction of the increasing  $y$ -axis and east is in the direction of the decreasing  $x$ -axis. The white arrow extending from the center of Peg III to the east is pointing in the direction of Psc II on the sky.

The normalized functional forms of the exponential and Plummer profiles are as follows:

$$\Sigma_{\text{exp}}(r_i) = \frac{1}{2\pi r_e^2 (1 - \epsilon)} \exp\left(-\frac{r_i}{r_e}\right), \quad (1)$$

$$\Sigma_p(r_i) = \frac{r_p^2}{2\pi(1 - \epsilon)} (r_i^2 + r_p^2)^{-2}. \quad (2)$$

Here,  $r_e$  and  $r_p$  are the scale lengths for each respective model, with  $r_e = 1.68a_h$  and  $r_p = a_h$ , and the first term in each equation is the normalization term, set to integrate to unity over all space. The  $r_i$  term is the elliptical radius of source  $i$ , defined as

$$r_i = \left\{ \left[ \frac{1}{1 - \epsilon} (X_i \cos\theta - Y_i \sin\theta) \right]^2 + (X_i \sin\theta + Y_i \cos\theta)^2 \right\}^{1/2}. \quad (3)$$

$X_i$  and  $Y_i$  are the spatial offsets from the centroid, where  $X_i = x_i - x_0$  and  $Y_i = y_i - y_0$ .

To calculate the best-fitting parameters, we used the Markov chain Monte Carlo (MCMC) ensemble sampler `emcee` (Foreman-Mackey et al. 2013). After adding the background surface density term, we fit the following two functions:

$$\Sigma_{\text{exp,tot}}(r_i) = \Sigma_{\text{exp}}(r_i) + \Sigma_b, \quad (4)$$

$$\Sigma_{p,\text{tot}}(r_i) = \Sigma_p(r_i) + \Sigma_b. \quad (5)$$

We created  $4''.5 \times 4''.5$  bins across the ACS FOV, masking the area of the chip gap and outside the FOV, and counted the number of stars in each bin. We chose this bin size as it was large enough that the highest surface density areas of these sparse galaxies contained more than one star per bin and small enough that it would not obscure any structural features. The

corner plots (Foreman-Mackey 2016) and posterior distributions for the exponential fits are shown in Figures 5 and 6 for Peg III and Psc II, respectively. For these and many subsequent figures, we choose to show plots using the exponential fit values as there are no considerable differences between the two profiles, and it allows easy comparison to what has already been presented in the literature. The values from this work and past works that measured structural parameters are shown in Tables 1 and 2, with the center position transformed from pixel space to coordinates in R.A. (RA) and decl. (DEC). The spatially binned, smoothed data, the smoothed best-fit exponential model, and the residuals are shown in Figures 7 and 8. For Peg III, the two most prominent residuals are in the NW and southeast (SE), with another to the southwest (SW). These show that a pure elliptical model cannot describe the full morphological complexity of Peg III. Psc II has prominent residuals to the north and NW, as well as one near the center of the image. We expect such small residual variation to be present even for models that reproduce the galaxy morphology.

The parameters of elliptical half-light radius and background surface density appear both correlated with the richness (number of stars) and with each other. The elliptical half-light radius has a positive correlation with the number of stars, while the background density has a negative correlation with the richness parameter. The elliptical half-light radius and background density parameters also have a negative correlation. One would expect the richness to increase with the elliptical half-light radius for a galaxy with the same central surface density ( $S_0$ ), as  $S_0$  is proportional to the richness divided by the squared scale radius, which in this case is the elliptical half-light radius. As the radius increases, for the  $S_0$  to remain the same, the richness must also increase. If the elliptical half-light radius is smaller, however, then a greater percentage of stars

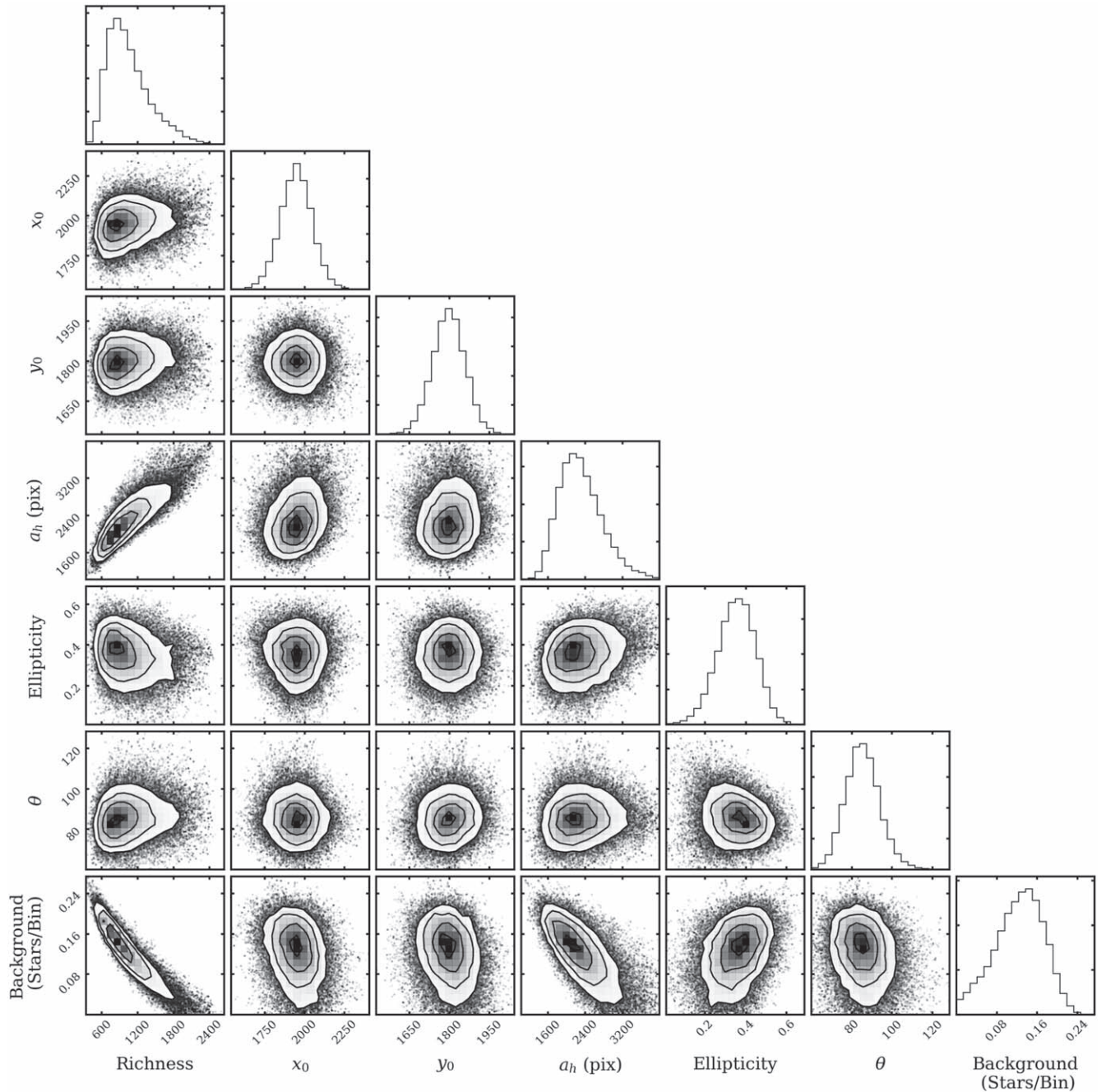


**Figure 5.** Corner plot for the Peg III structural parameters from the exponential fit. Positive correlations exist between the richness (number of stars) and elliptical half-light radius as well as the elliptical half-light radius and ellipticity. There is a negative correlation between the richness and background density.

within the FOV would be expected to belong to the background. Similarly, for a given number of stars within an FOV, if a higher percentage of stars belongs to the galaxy, then a lower number will be attributed to the background.

We show the best-fitting exponential and Plummer profiles for each galaxy (left: Peg III, right: Psc II) in Figure 9. Surface density measurements taken at 0.1 increments of the elliptical half-light radius are plotted against the elliptical radius  $R_e$  of each annular bin.

While the structural parameters we measured for Psc II are consistent with previous literature values, the  $a_h$  value of Peg III ( $1.88^{+0.42}_{-0.33}$ ) is much larger ( $\sim 2.2\times$ ) than the most recent literature value from Kim et al. (2016) ( $0.85 \pm 0.22$ , referred to as  $r_h$  in their paper). This can be seen in the leftmost panel of

Figure 10. Here, we illustrate the best-fit 2D-exponential models projected onto the sources in our FOV. The best-fit Plummer model from this work is shown as the dashed ellipse. Both the Kim et al. (2015, 2016) structural fits show the semimajor axis extending in the SE to NW direction, while our fits extend more along the east to west axis. The NW overdensity in our Figure 4 and smoothed data and residuals in Figure 7 could have affected the Kim et al. fits. The same best-fit 2D-model comparisons are shown for Psc II, with the exponential fits shown in the middle panel and the Plummer fits in the right panel.

As discussed in Muñoz et al. (2012), the FOV should be at least  $3\times$  the half-light radius (assuming circular symmetry) in order to measure the morphology to 10% accuracy. With the



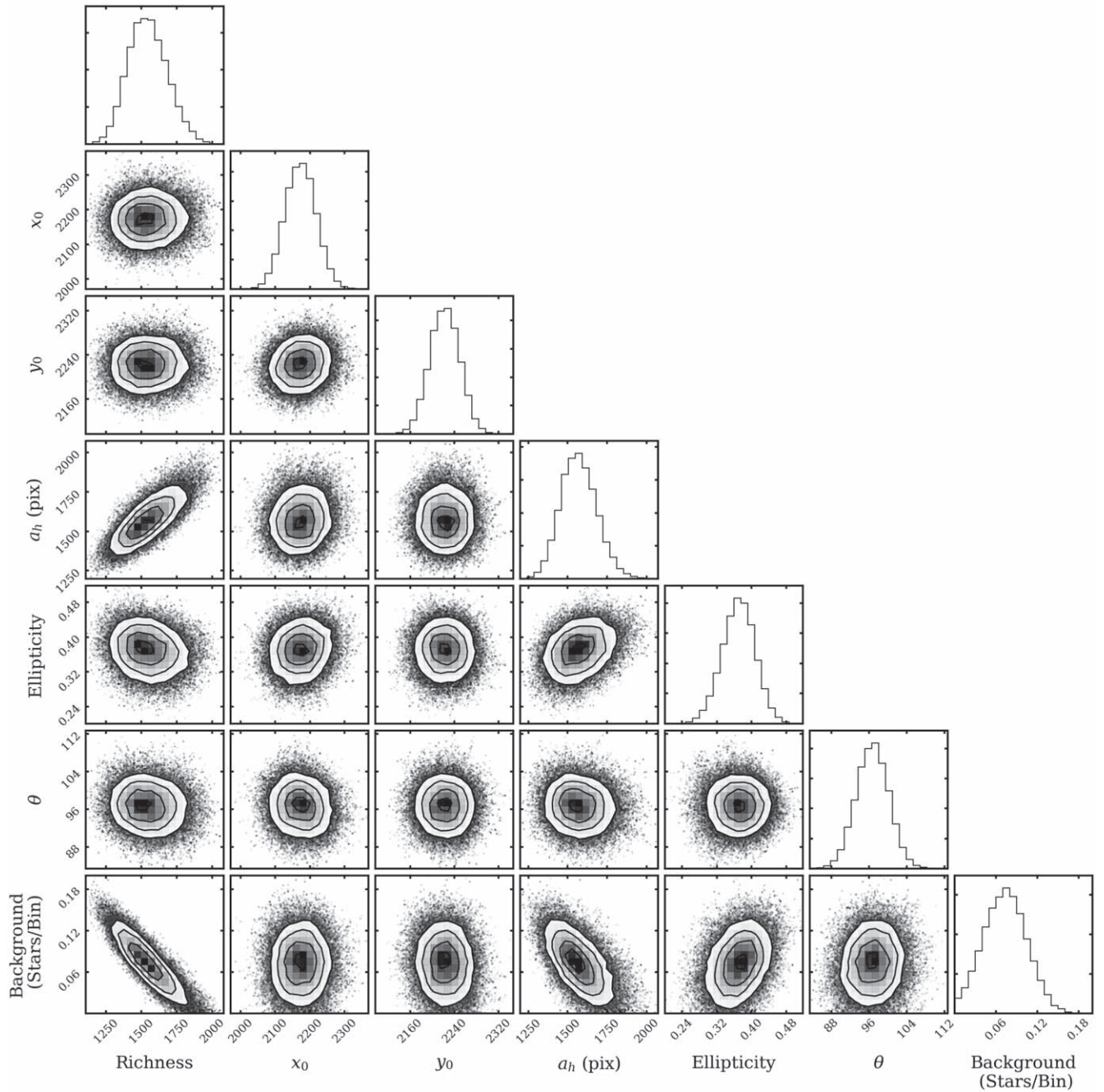


Figure 6. Same as Figure 5, but for Psc II.

ACS FOV width of  $202''$ , or  $3/36$ , we cover approximately  $3.96\times$  the  $0'.85$  value for the elliptical half-light radius that we expected based on Kim et al. (2016). However, when compared to our measured values for Peg III, the ACS FOV is  $\sim 1.8\times$  our exponential  $a_h$  and  $\sim 2.5\times$  our Plummer  $a_h$ . For Psc II, the ratios are  $\sim 2.6\times$  and  $\sim 2.5\times$  for the exponential and Plummer  $a_h$  values, respectively. We explore trends in the structural parameters as a function of  $a_h$  to FOV ratio in the next subsection.

### 3.2. Mock Galaxy Tests

To test how well our fitting procedure could recover the elliptical half-light radius for a galaxy given a limited FOV, we created simulated galaxies in Cartesian space based on the

best-fit values for Peg III. After generating distributions based on the probability density functions of the Plummer and exponential models, we randomly drew stars to match the length of the final Peg III catalog and added a set number of background stars matching the best-fit background density value. These simulated data were then masked with the ACS FOV and chip gap and run through the MCMC sampler. The results of these tests are shown in Figure 11.

From this, we see that the code can recover  $a_h$  up to  $\sim 1'.4$  before it begins to return larger than the input  $a_h$  values. Even up to  $1'.8$ , however, the expected  $a_h$  values fall within the uncertainties for both models, and remain close through  $2'.5$ . Our measured  $a_h$  values for Peg III of  $1'.88$  and  $1'.67$  for the exponential and Plummer profiles, respectively, could therefore

**Table 1**  
Absolute Magnitude and Structural Properties for Peg III

Peg III			
Parameter	Kim et al. (2015)	Kim et al. (2016)	This Work
$M_V$	$-4.1 \pm 0.5$	$-3.4 \pm 0.4$	$-4.17^{+0.19}_{-0.22}$
Exponential			
R.A. (h:m:s)	$22:24:22.6 \pm 15''$	22:24:24.48	$22:24:25.82 \pm 5''$
DEC (d:m:s)	$+05:25:12 \pm 14''$	+05:24:18.0	$+05:24:54.01 \pm 3''$
$\theta_{\text{exp}}$ (deg)	$133 \pm 17$	$114^{+19}_{-17}$	$85 \pm 8$
$\epsilon_{\text{exp}}$	$0.46^{+0.18}_{-0.27}$	$0.38^{+0.22}_{-0.38}$	$0.36^{+0.09}_{-0.10}$
$a_{h,\text{exp}}$ (arcmin)	$1.3^{+0.5}_{-0.4}$	$0.85 \pm 0.22$	$1.88^{+0.42}_{-0.33}$
$a_{h,\text{exp}}$ (pc)	$78^{+30}_{-24}$	$53 \pm 14$	$118^{+31}_{-30}$
Plummer			
RA (h:m:s)	...	...	$22:24:25.78 \pm 5''$
DEC (d:m:s)	...	...	$+05:24:54.17 \pm 3''$
$\theta_p$ (deg)	...	...	$83^{+8}_{-7}$
$\epsilon_p$	...	...	$0.37^{+0.08}_{-0.09}$
$a_{h,p}$ (arcmin)	...	...	$1.67^{+0.26}_{-0.21}$
$a_{h,\text{exp}}$ (pc)	...	...	$104^{+20}_{-23}$

**Note.** The top six lines report the absolute V-band magnitude and best-fit exponential values, and the bottom five list the best-fit Plummer values. The uncertainties reported for RA, DEC,  $\theta$ ,  $\epsilon$ , and  $a_h$  in arcminutes are the 16th and 84th percentiles from the MCMCs. The uncertainties on  $M_V$  and  $a_h$  in parsecs are the 16th and 84th percentiles from Monte Carlo (MC) simulations that took into account the errors on the distance modulus. Kim et al. (2015) and Kim et al. (2016) did not fit Plummer profiles to their data, and Kim et al. (2016) did not provide uncertainties on their central positions.

be taken as upper limits on the true value. The maximum well-recovered value of  $\sim 1'.4$  extending beyond the previously reported  $a_h = 0'.85$  (Kim et al. 2016) suggests that our modeling would have been able to capture if Peg III was indeed so compact.

### 3.3. Apparent and Absolute V-band Magnitude Calculations

To derive the integrated magnitudes of each UFD, we opted for a probabilistic model approach as opposed to using discrete stars. To begin, we selected a box in color–magnitude space from  $0 \leq (V - I) \leq 1.2$  and  $20 \leq m_V \leq 29$ , as this encompassed the majority of stars from the CMD that would be expected to belong to the galaxies. For both the on-field and off-field, we created a Gaussian kernel using `scikitlearn` (Pedregosa et al. 2012) `Kernel Density` and fit the kernel to the stars inside the color–magnitude box (CMD box). We gridded this space into 100 bins along each dimension, resulting in color bins  $\sim 0.01$  dex and magnitude bins  $\sim 0.1$  dex in width. We then generated random samples from the on- and off-field kernels and computed the log-likelihood of each sample under the model. The off-field was used to create a probabilistic background model from which we estimated the excess flux. Integrating in both color and magnitude space, we calculated the stellar density in the CMD box by multiplying the log-likelihoods by the area of the CMD box and subtracting the off-field model from the on-field. The integral returned the flux of the stars inside the CMD box. We multiplied this flux by a correction factor derived from the exponential models to account for the flux outside the FOV. Converting this flux back to magnitude space yielded the integrated apparent magnitude.

This calculation was performed within an MC simulation that included the individual source magnitude errors and FOV corrections calculated from different sets of model parameters. We report the median integrated  $m_V$  values of  $17.50^{+0.15}_{-0.21}$  and  $17.03 \pm 0.04$  for Peg III and Psc II, respectively, with the uncertainties representing the 16th and 84th percentiles. For the integrated  $M_V$ , we performed the same MC simulation, this time also including errors on the distance modulus. We used the Kim et al. (2016) value of  $21.66 \pm 0.12$  for Peg III and the Sand et al. (2012)  $21.31 \pm 0.17$  value for Psc II. The most recent distance estimates (Garofalo et al. 2021) indicate that the two UFDs have more similar heliocentric distances (Peg III  $\sim 174$  kpc; Psc II  $\sim 175$  kpc); however, our CMDs shown in Figure 3 suggest that Peg III is farther away than Psc II, as the horizontal branch and main-sequence turnoff for Peg III are both  $>0.5$  magnitudes less bright than those of Psc II. As such, we chose to move forward with the previously reported literature values in our MC simulations, which gave the median  $M_V = -4.17^{+0.19}_{-0.22}$  for Peg III and  $-4.28^{+0.19}_{-0.16}$  for Psc II, with the 16th and 84th percentiles quoted as the uncertainties.

### 3.4. Mass-to-light Ratios

Using the newly derived elliptical half-light radii values, we calculate updated mass values using velocity dispersion values from Kirby et al. (2015) and Kim et al. (2016). We use Equation (6) derived by Wolf et al. (2010), which was also employed by Kim et al. (2016) to estimate the mass within the elliptical half-light radius of Peg III.  $R_e$  is defined as the 2D-projected half-light radius from elliptical fits of surface brightness profiles and aligns with our  $a_h$  values.

$$M_{1/2} \simeq \frac{4}{G} \sigma_v^2 R_e. \quad (6)$$

The Kim et al. (2016)  $\sigma_v = 5.4^{+3.0}_{-2.5}$  km s $^{-1}$ , determined using seven member stars, and our elliptical half-light radius measurement of 118 pc at 215 kpc gives a  $M_{1/2} = 3.2^{+4.3}_{-2.1} \times 10^6 M_\odot$  for Peg III. Converting our  $M_V$  value to luminosity, we obtain the mass-to-light ratio within the elliptical half-light radius ( $(M/L_V)_{1/2} = 1600^{+480}_{-580} M_\odot / L_\odot$ ). This is within  $1\sigma$  of the previously derived  $1470^{+5660}_{-1240} M_\odot / L_\odot$  from Kim et al. (2016). Using the Kirby et al. (2015)  $\sigma_v = 5.4^{+3.6}_{-2.4}$  km s $^{-1}$ , which was also calculated using seven member stars, and our elliptical half-light radius of 69 pc at 183 kpc, we calculate a  $M_{1/2} = 1.9^{+3.3}_{-1.3} \times 10^6 M_\odot$  for Psc II. The  $(M/L_V)_{1/2}$  is then  $850^{+570}_{-260} M_\odot / L_\odot$ . This agrees within  $2\sigma$  with the value of  $370^{+310}_{-240} M_\odot / L_\odot$  that Kirby et al. (2015) derived.

## 4. Orbital Analysis

### 4.1. Previous Literature

Kim et al. (2015) and Kim et al. (2016) hypothesized a connection between Peg III and Psc II immediately upon the discovery of the former, due at first to their small on-sky separation ( $8^\circ 5$ ), LOS separation of  $\sim 32$  kpc, and similar heliocentric distances, and later from their similar radial velocities and calculated physical separation of  $\sim 36$  kpc. Kim et al. (2016) also noted the presence of an irregularity in the isodensity lines for Peg III in the direction of Psc II, but included the caveat of small number statistics.



**Table 2**  
Same as Table 1, but for Psc II

Parameter	Psc II			
	Belokurov et al. (2010)	Sand et al. (2012)	Muñoz et al. (2018)	This Work
$M_V$	$-5.0 \pm 0.5$	$-4.1 \pm 0.4$	$-4.22 \pm 0.38$	$-4.28^{+0.19}_{-0.16}$
		Exponential		
RA (h:m:s)	...	$22:58:32.33 \pm 5''$	$22:58:32.28 \pm 9''15$	$22:58:32.76 \pm 2''$
DEC (d:m:s)	...	$+05:57:17.7 \pm 4''$	$+05:57:09.36 \pm 5''7$	$+05:57:20.36 \pm 1''$
$\theta_{\text{exp}}$ (deg)	...	107	$98 \pm 13$	$97 \pm 3$
$\epsilon_{\text{exp}}$	...	$<0.28$	$0.39 \pm 0.10$	$0.37 \pm 0.04$
$a_{h,\text{exp}}$ (arcmin)	...	$1.09 \pm 0.19$	$1.18 \pm 0.20$	$1.31^{+0.10}_{-0.09}$
$a_{h,\text{exp}}$ (pc)	...	$58 \pm 10$	$62.5 \pm 10.6$	$69 \pm 8$
		Plummer		
RA (h:m:s)	$22:58:31 \pm 6''$	$22:58:32.20 \pm 5''$	$22:58:32.28 \pm 9''15$	$22:58:32.75 \pm 2''$
DEC (d:m:s)	$+05:57:09 \pm 4''$	$+05:57:16.3 \pm 4''$	$+05:57:09.36 \pm 5''7$	$+05:57:19.96 \pm 1''$
$\theta_p$ (deg)	$77 \pm 12$	$110 \pm 11$	$78 \pm 20$	$98 \pm 3$
$\epsilon_p$	$0.4 \pm 0.1$	$0.33 \pm 0.13$	$0.34 \pm 0.10$	$0.37^{+0.03}_{-0.04}$
$a_{h,p}$ (arcmin)	$1.1 \pm 0.1$	$1.12 \pm 0.18$	$1.12 \pm 0.16$	$1.34^{+0.08}_{-0.07}$
$a_{h,p}$ (pc)	$58 \pm 5^*$	$60 \pm 10$	$59.3 \pm 8.5$	$71 \pm 8$

**Note.** Belokurov et al. (2010) did not fit an exponential model to their data. Sand et al. (2012) had unconstrained uncertainties for the position angle in their exponential model and their reported ellipticity is the 68% upper confidence limit. \*The uncertainty on the  $a_h$  in parsecs was derived for this work from an MC simulation using the uncertainty on the  $a_h$  in arcminutes and the distance modulus of 21.3 reported in Belokurov et al. (2010).

Focusing on the ellipticity of Peg III, which we find to be  $0.36^{+0.09}_{-0.10}$ , Kim et al. (2016) considered that, if not caused by the formation process, this could be the result of tidal interactions with the MW, a more likely scenario if Peg III is not in dynamic equilibrium or if unresolved binaries are inflating the velocity dispersion. In such a case, they suggested that Peg III might be a tidally disrupted dwarf galaxy remnant but would need to have had a highly eccentric orbit to achieve close enough Galactocentric distances to experience tidal effects. Alternatively, the ellipticity of Peg III could have been caused by a tidal interaction with Psc II, though at the time, there was not enough orbital information for Kim et al. (2016) to further investigate this possibility. While our mass estimate for Peg III is greater than that of Psc II, Kim et al. (2016) measured Peg III to be  $0.85$  and thus smaller than Psc II, which could explain why they suggested Peg III could have been tidally affected by Psc II.

#### 4.2. PM Measurements

Recently, several authors have measured the PMs of Peg III and Psc II using data from Gaia eDR3 (McConnachie & Venn 2020; Battaglia et al. 2021; Li et al. 2021), now making it possible to explicitly calculate the orbital histories of both galaxies simultaneously to assess whether or not they could be or have been a bound pair.

Li et al. (2021) reported a PM for Psc II using three stars and found a highly eccentric orbital history such that Psc II only reaches its closest distance relative to the MW at its current distance. By integrating both forward and back for 10 Gyr, they also concluded that Psc II shows a high probability of being unbound from the MW's halo (95.85%).

Battaglia et al. (2021) independently measured the PM of Psc II using two member stars from Gaia eDR3, and though they measured a different PM for Psc II and included the infall of a massive LMC in their models, their measurements still implied that Psc II is not and has never been bound to the MW.

Both Battaglia et al. (2021) and Li et al. (2021) tested a similar range of MW mass models to arrive at these conclusions.

McConnachie & Venn (2020) reported the first PM value for Peg III measured using only one member star, in addition to their own estimate for the PM of Psc II using four spectroscopic member stars, three of which had radial velocities more than  $3\sigma$  away from the mean velocity of the system. The reported uncertainties were smaller than those of Li et al. (2021) and Battaglia et al. (2021) by a factor of 2 or more. However, unlike Li et al. (2021) and Battaglia et al. (2021); McConnachie & Venn (2020) imposed a prior on their PM determinations such that the galaxies are assumed to be bound to the MW (in direct contrast to the orbital histories suggested by the Battaglia et al. (2021) and Li et al. (2021) PMs). Given that Peg III and Psc II are outer MW dwarfs, such a restrictive prior biases the measured PMs toward zero. In this work, we calculated orbital histories using the McConnachie & Venn (2020) PMs (see Table 3) for both galaxies given the uniform methodology that yields PMs with the lowest reported uncertainties for both dwarfs, keeping in mind that the prior could affect the resulting orbital histories and subsequent interpretations.<sup>20</sup>

#### 4.3. Orbital Model and Results

Here, we explore whether the two UFDs could have interacted with each other, with the MW, or with the LMC. Radial velocities are adopted from Kim et al. (2016; Peg III) and Kirby et al. (2015; Psc II) and distance moduli<sup>21</sup> are

<sup>20</sup> Following the initial submission of this paper, Pace et al. (2022) measured new systemic proper motions for Peg III and Psc II using the structural parameters reported herein. Their measurements agree with the McConnachie & Venn (2020) values used in our orbital analysis within one to two sigma.

<sup>21</sup> During the course of the analysis for this paper, new distance measurements were published by Garofalo et al. (2021), derived using RR Lyrae. The range of errors we considered in the distance moduli for the orbital analysis spans a large portion of their values of  $174 \pm 18$  kpc for Peg III and  $175 \pm 11$  kpc for Psc II, thus we did not perform separate calculations here because the PM error space is by far the dominant source of measurement uncertainties.

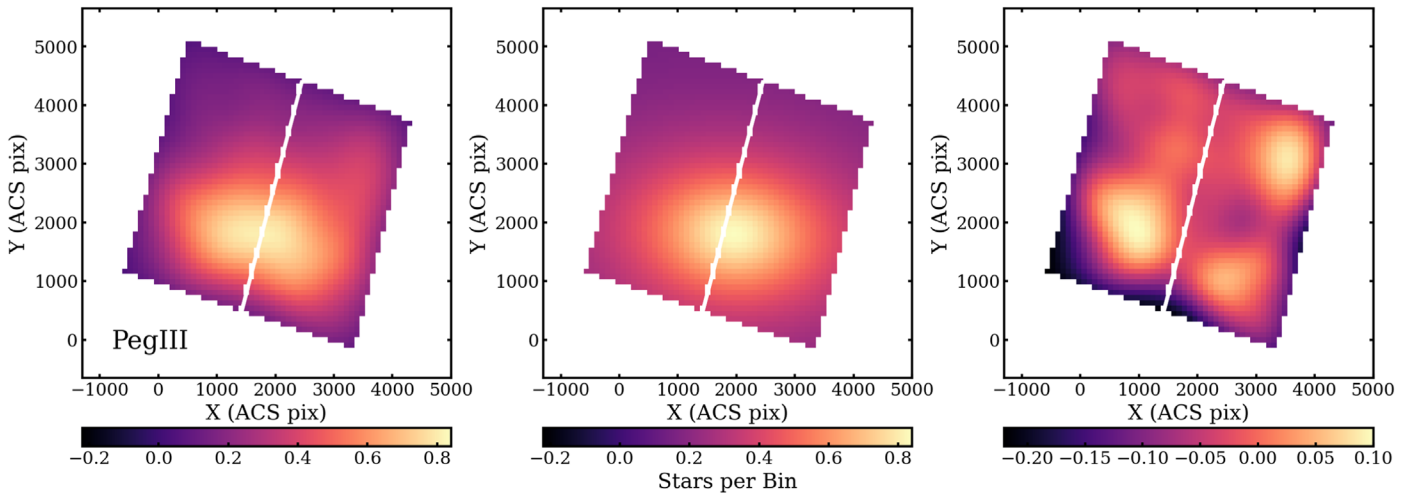


**Figure 7.** Left: Peg III data, smoothed using a Gaussian kernel with an FWHM of  $0''.5$ . Middle: best-fitting exponential model, smoothed with a  $0''.5$  FWHM Gaussian kernel. Right: the residuals between the smoothed data and the model.

adopted from Kim et al. (2016; Peg III) and Sand et al. (2012; Psc II), respectively. Direct orbital histories are calculated using initial phase-space coordinates that equal the direct transformation of PMs, LOS velocity, and distance converted to Galactocentric phase-space coordinates.

Following the methodology of Patel et al. (2020), we integrate orbits for Peg III and Psc II in a three-component (Hernquist bulge + Miyamoto–Nagai disk + NFW (Navarro–Frenk–White) halo) MW-only potential and a combined three-component MW and two-component (Miyamoto–Nagai disk + NFW halo) LMC potential using a fixed LMC mass of  $1.8 \times 10^{11} M_{\odot}$ , which was used as the fiducial model in Patel et al. (2020) and is consistent with abundance-matched halo estimates and recent Magellanic system models (e.g., Guo et al. 2011; Besla et al. 2012, 2013, 2016) based on empirical measurements and dynamical mass arguments (e.g., Kim et al. 1998; Majewski et al. 2009; Saha et al. 2010; van der Marel & Kallivayalil 2014; Mackey et al. 2016). Here, the MW is allowed to move in response to the LMC’s gravitational influence. Two MW masses are considered: MW1 has a virial mass of  $10^{12} M_{\odot}$ , while MW2 has a virial mass of  $1.5 \times 10^{12} M_{\odot}$ . Peg III and Psc II are modeled as Plummer spheres with a total mass of  $10^9 M_{\odot}$  and a Plummer scale radius of 1 kpc (Jeon et al. 2017). Dynamical friction owing to the MW and the LMC is also included, as in Patel et al. (2020). See Patel et al. (2020) Tables 3 and 4 for all MW and LMC model parameters.

One important difference with respect to the methodology of Patel et al. (2020) is that we have explicitly accounted for the gravitational forces that Peg III and Psc II exert on each other, as it has been speculated that they may be a bound pair. Thus, we calculate the joint, four-body orbital history of the MW, LMC (when applicable), Peg III, and Psc II. We have also checked whether including the additional gravitational influence of the SMC is significant and find that the SMC negligibly affects the orbits of Peg III and Psc II, thus we do not incorporate it in the rest of this analysis.

The direct orbital histories of Peg III (cyan) and Psc II (magenta) using the McConnachie & Venn (2020) PM values are shown in Figure 12. These orbits do not represent the uncertainties in the measured quantities (i.e., distance, PM,

LOS velocity). Uncertainties on the orbital parameters that do account for such are provided in Tables 4 and 5.

Orbital histories with respect to the MW (top panel, Figure 12) in the MW-only potential (dashed lines) indicate that both Peg III and Psc II complete a very close ( $\leq 20$  kpc), pericentric approach around the MW at  $\sim 2.5$  Gyr (MW1) or  $\sim 2$  Gyr ago (MW2). However, when the influence of the LMC is included, the satellites complete a pericentric approach around the MW at  $\sim 1.5$  Gyr ago in both MW mass models at distances of  $\sim 50$ – $90$  kpc. Thus, the influence of the LMC significantly increases the distance at the pericenter about the MW and changes the timing at which the pericenter occurs. This effect is twofold as it is caused by the gravitational influence of the LMC itself in addition to the LMC causing the MW’s center of mass to move in response to the passage of the LMC. We also test LMC masses in the range  $8$ – $25 \times 10^{10} M_{\odot}$  and find no significant differences in the resulting orbital histories.

These results are in contrast to the role the LMC plays on the orbit of Crater 2, for example, where including the LMC plunges Crater 2 further into the halo of the MW, providing a possible explanation for its puffed up morphology (Torrealba et al. 2016; Caldwell et al. 2017; Fritz et al. 2018; Fu et al. 2019; Ji et al. 2021). Peg III and Psc II are much more compact than Crater 2, however, and are thus much less vulnerable to tidal effects. In upcoming work, we will further disentangle which physical effects associated with the passage of the LMC (i.e., the formation of the dark-matter wake, the large-scale density perturbations introduced to the MW dark-matter halo, or LMC tidal debris) are most significant for altering the orbital histories of low-mass satellite companions in the MW’s halo (E. Patel et al. 2022, in preparation). Indeed, in our density contour maps (Figure 4) and in the recent Garofalo et al. (2021) paper, there appear to be no signs of tidal effects, and while our Peg III elliptical half-light radius is larger than previous literature values, it is still an order of magnitude smaller than that of Crater 2 ( $\sim 118$  pc compared to  $\sim 1100$  pc; Torrealba et al. 2016).

The middle panels of Figure 12 show the orbits of Peg III and Psc II with respect to the LMC as the LMC also falls into the halo of the MW. The orbits of the two UFDs are very similar to each other and exhibit a pericentric passage about the

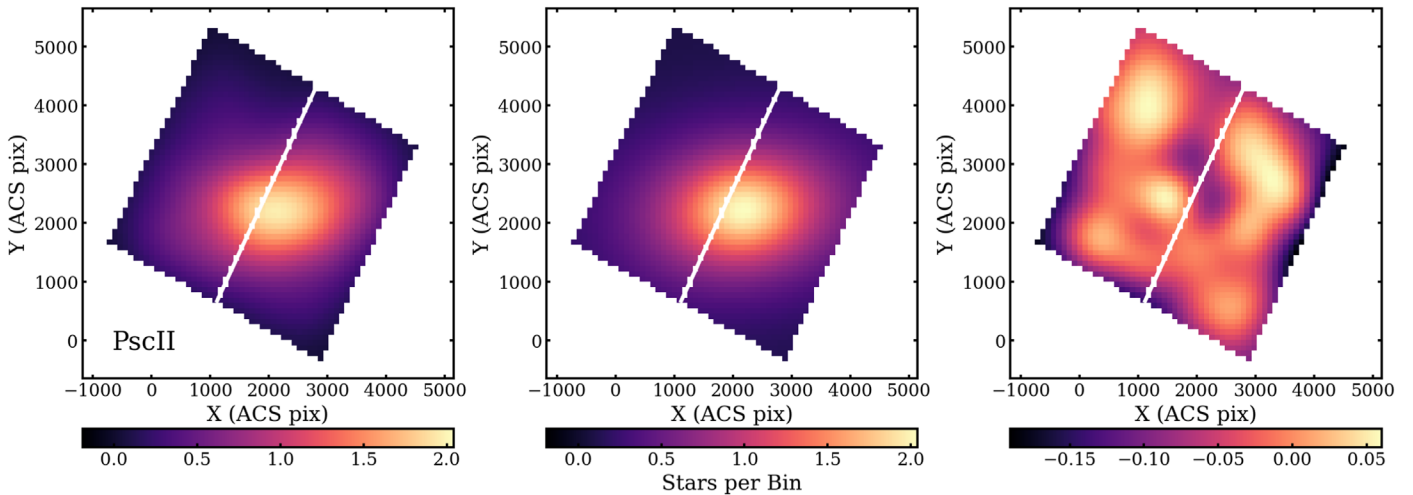


**Figure 8.** Left: Psc II data, smoothed using a Gaussian kernel with an FWHM of  $0''.5$ . Middle: best-fitting exponential model, smoothed with a  $0''.5$  FWHM Gaussian kernel. Right: the residuals between the smoothed data and the model.

LMC at about 0.8 Gyr ago at  $\sim 30$  kpc for MW1 and  $\sim 60$  kpc for MW2. This yields further evidence that the dynamics of the UFDs have been strongly impacted by the gravitational influence of the LMC, even if they are not in close proximity to the LMC at present (Peg III is 219 kpc from the LMC and Psc II is 195 kpc from the LMC). It is unclear whether the satellites were ever bound to the LMC based on the calculations presented here. Note that for MW1, the LMC’s median infall time is approximately 1.4 Gyr ago and about 7 Gyr ago for MW2 (Patel et al. 2017). Despite this large variation in infall time for the LMC, the UFDs behave fairly similarly over the last  $\sim 3$  Gyr in both MW mass potentials.

In addition to computing the direct orbital histories, we also assess how much the measurement uncertainties in PM, LOS velocity, and distance affect the corresponding orbital histories for Peg III and Psc II. To this end, we calculate 1000 orbits for each orbital model: light MW-only, heavy MW-only, light MW+LMC, heavy MW+LMC. These 1000 orbits use initial conditions drawn in an MC fashion from the  $1\sigma$  uncertainty on PM, LOS velocity, and distance for each dwarf galaxy (plus the LMC when included); thus, the phase-space uncertainties for both galaxies are jointly sampled in the three-body and four-body calculations.

In Tables 4 and 5 we list the distance and timing of pericenter and apocenter for the representative direct orbital histories in Figure 12. We use the direct values because the mean and median obtained from the MC distribution can be biased toward larger values, especially for the apocenter (see Fritz et al. 2018). The uncertainties provided correspond to the 16th and 84th percentiles around the median of the distributions resulting from 1000 orbit calculations spanning the uncertainty in phase-space coordinates. We report orbital parameters for each satellite with respect to the MW, LMC, and each other for both MW mass models. Note that orbital parameters are only listed for the fraction of orbits where a pericenter<sup>22</sup> (or apocenter) is recovered along the orbital trajectory. Therefore, the uncertainties do not encompass the

orbital histories where no such critical minima and maxima are recovered in the last 6 Gyr.

#### 4.4. Caveats

As we do not account for the evolving MW potential or large-scale structure, we only integrate orbits for the last 6 Gyr. Furthermore, it has been shown that the LMC significantly perturbs the shape and density of the MW’s dark-matter halo, loses a significant portion of its own mass, and creates a trailing wake of dark matter over the last  $\sim 2$  Gyr (Garavito-Camargo et al. 2019, 2021). Thus, the most physically accurate model of Peg III and Psc II’s orbital histories would be calculated in a time-evolving MW+LMC potential accounting for such features (D’Souza & Bell 2022; E. Patel et al. 2022, in preparation). Given the significant PM uncertainties and the complex dynamics of the MW-LMC system, we note that the orbits presented here are only an approximation of the most plausible orbital histories within the measured phase space of these dwarf galaxies, assuming they are indeed bound to the MW (as imposed by the prior in McConnachie & Venn 2020).

## 5. Discussion

### 5.1. Comparison to Simulations and Other UFDs

Peg III and Psc II are among the few known UFDs in the outer halo of the MW, at Galactocentric distances of  $\sim 213$  and  $\sim 182$  kpc, respectively. To see how our measured Peg III and Psc II azimuthally averaged half-light radius ( $r_h$ ) and  $M_V$  values compare with those of other faint MW satellites, we place them in a size–luminosity plane (Figure 13). In addition to observed MW satellites (with  $a_h$  converted to  $r_h$  where necessary; McConnachie 2012; Muñoz et al. 2018), we have also included values from five sets of simulated UFDs: Jeon et al. (2017, 2021a, 2021b); Wheeler et al. (2019), and Applebaum et al. (2021). The observed satellites are split between two panels to explore the difference between those closer (left;  $< 100$  kpc) and farther (right;  $> 100$  kpc) from the Galactic Center. The simulated galaxies are shown in both panels, except for the Applebaum et al. (2021) values, which are split between the two according to the Galactocentric distances determined within their framework.

<sup>22</sup> Note that some studies will adopt the minimum relative distance when no critical minimum is recovered (e.g., Battaglia et al. 2021); however, we do not follow this methodology as the minimum distance does not always correspond to a true pericentric passage.



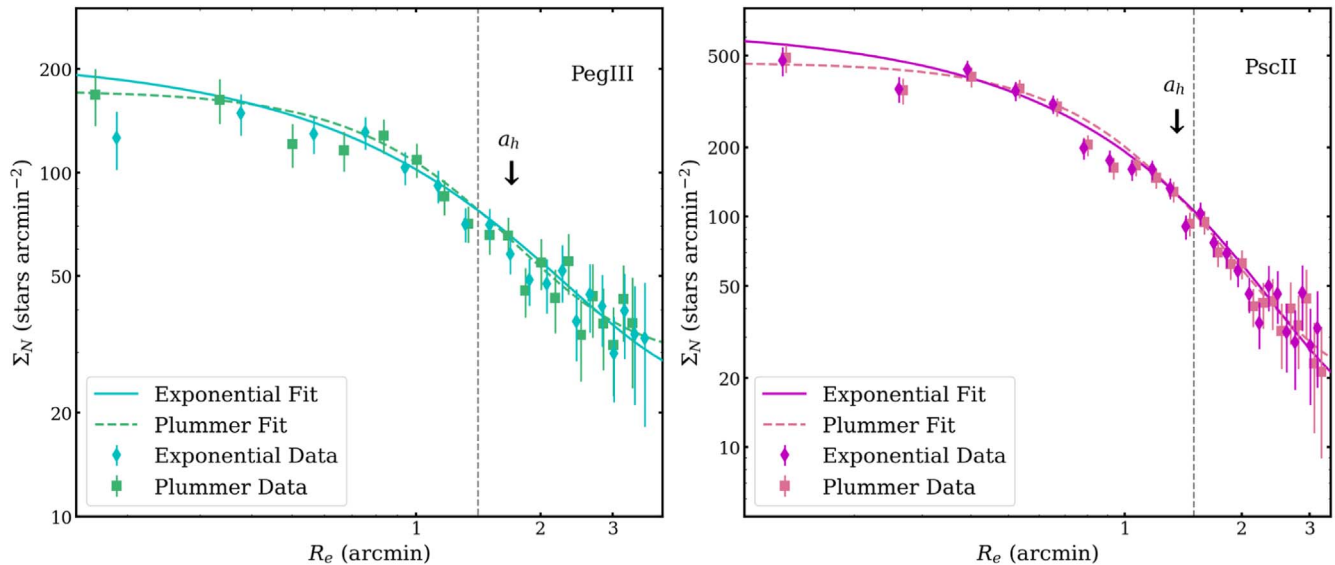


**Figure 9.** Best-fitting models for the surface density profiles of Peg III (left) and Psc II (right) plotted against the elliptical radius. The curves show the best-fit one-dimensional exponential (solid) and Plummer (dashed) profiles, which are fit to the full stellar distribution, not the annularly binned data shown here. The gray dashed line marks the approximate point where the elliptical annuli used for the surface density measurements begin to cover area outside the FOV in pixel space without source information in our catalogs. This was corrected for by dividing the number of stars in each elliptical annulus by only the area overlapping the FOV. The diamonds (squares) represent the surface density measurements in bins using the exponential (Plummer) model, with elliptical radii in increments of  $0.1a_h$ . The errors come from a Poisson distribution.  $a_h$  marks the data points corresponding to the best-fit elliptical half-light radius.

To derive  $M_V$  values for the Jeon et al. and Wheeler et al. (2019) simulations, we used *Starburst99* (Leitherer et al. 1999) to convert from stellar mass, based on the Padova evolutionary tracks (Bressan et al. 1993; Fagotto et al. 1994a, 1994b; Girardi et al. 2000), and the given half-stellar-mass radii as (circular) half-light radii. The half-light radii that Applebaum et al. (2021) report are circular and derived from the summation of particle luminosities.

The Wheeler et al. (2019) simulations were unable to produce UFDs with half-light radii lower than 200 pc, which the authors suggested could be in tension with current observations because telescopes might only be sensitive to the *bright* cores of diffuse and relatively massive objects. Similarly, the Applebaum et al. (2021) simulations did not produce any galaxies in the UFD magnitude range with smaller  $r_h$  than  $\sim 300$  pc, which may have been due to their force softening. Among the simulations included in our comparison, the Wheeler et al. (2019) and Jeon et al. (2021a, 2021b) simulations have the highest resolution, with Wheeler et al. using  $m_{\text{gas}} = 30$  and  $m_{\text{gas}} = 250 M_\odot$  in their high- and medium-resolution simulations, respectively, and Jeon et al. using  $m_{\text{gas}} \sim 60 M_\odot$ . As simulation techniques improve and are able to resolve a broader diversity of UFDs in an MW environment, it will be interesting to see whether they more closely reproduce the scatter shown by McConnachie (2012) and Muñoz et al. (2018).

For Figure 13, we have imposed an upper magnitude limit of  $M_V = -7.7$  to only include simulated galaxies in the UFD range, as Jeon et al. (2017), Wheeler et al. (2019), and Applebaum et al. (2021) produced galaxies in the dSph regime as well. As seen in Figure 13, Peg III and Psc II are well within the observed  $M_V$  and  $r_h$  ranges for other MW UFDs. They also fall in the range covered by the Jeon et al. (2021a, 2021b) simulated field UFDs. Some closer MW UFDs and MW UFD candidates also fall within the simulated field UFD area, suggesting against this agreement being unique to outer-halo UFDs. Additionally, there is a higher number of observed

satellites with smaller  $r_h$  and fainter  $M_V$  within 100 kpc, likely due to observational constraints.

As new observatories come online with deeper detection limits, smaller and fainter satellites beyond 100 kpc could be discovered that have no analogs in current simulations. One might expect outer-halo satellites that have never been within 100 kpc of the MW to be more compact than UFDs with similar masses that have been closer and possibly subjected to strong tidal forces. If there are no or very few distant UFDs found in this smaller and fainter regime, the impact of the LMC and how it might have drawn UFDs closer ( $\sim 50$  kpc) at some point in their orbital history could be considered. While our orbital histories for Peg III and Psc II show the LMC increasing the pericenter distance, it is possible that other MW satellites (e.g., Crater 2, Ji et al. 2021) could have experienced very different effects.

## 5.2. A Bound Pair?

Several proposed pairs of galaxies have been reported within the Local Group (Pawlowski 2021). Speculation that Peg III and Psc II are associated began in the Peg III discovery paper (Kim et al. 2015), due to their on-sky proximity and spatial separation of  $\sim 30$  kpc. The support for this association increased with the Kim et al. (2016) measurement of a radial velocity for Peg III within  $\sim 10 \text{ km s}^{-1}$  of that of Psc II. Additionally, they found the same irregularity in structure in their deeper imaging as in the discovery paper.

The next work to investigate the possible connection between Peg III and Psc II was Garofalo et al. (2021). Using LBT data, they found no irregular shape and concluded that there were no signs of past tidal interactions. In our density contour maps (Figure 4), we find no signs of an irregular shape for Peg III (unlike Kim et al. 2015, 2016) or for Psc II, which we calculated to be the less massive of the two UFDs and therefore possibly more susceptible to tidal effects. While previously limited to only looking at the morphologies for hints

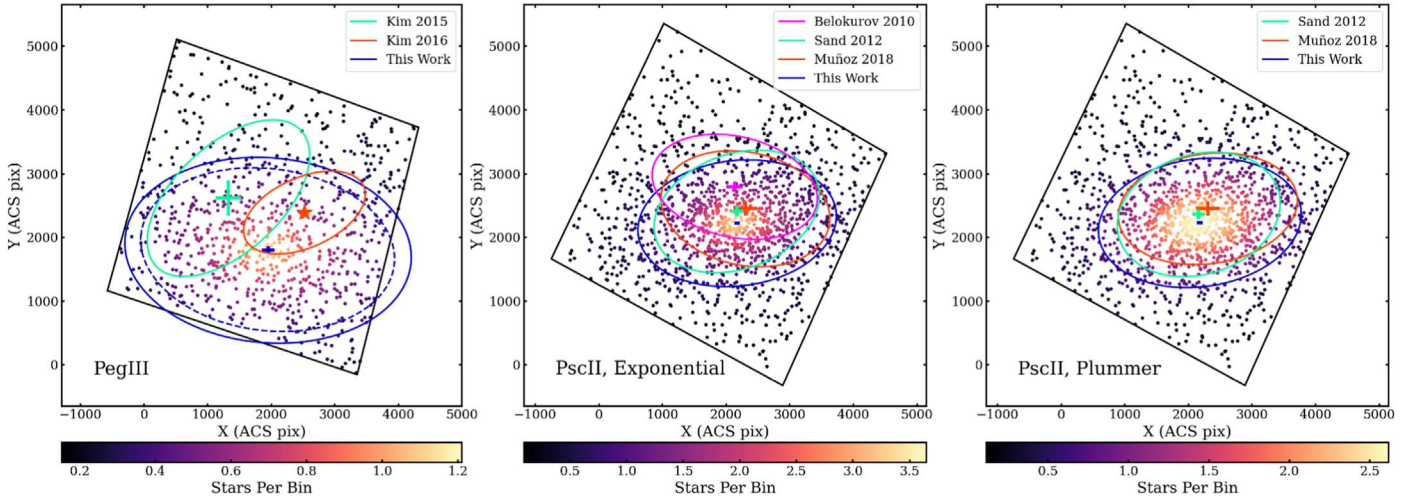


**Figure 10.** Comparison of past literature fits. Individual sources are colored based on the binned surface densities of the best-fitting exponential models in the left and center panels and the best-fitting Plummer model in the right panel. Left: Peg III exponential profile fits from Kim et al. (2015) and Kim et al. (2016) are shown in green and orange, respectively. The exponential profile fit from this work is shown in solid blue. The Plummer fit from this work is shown as the dashed blue ellipse. The central position is shown with error bars for Kim et al. (2015) in green and for this work’s exponential fit in blue. The central position from this work’s Plummer fit is not shown as it almost completely overlaps with the exponential value. The central position from Kim et al. (2016) is marked with an orange star, as no errors were reported. Middle: exponential profile fits and central positions with error bars for Psc II. Belokurov et al. (2010) is shown in fuchsia, Sand et al. (2012) in green, Muñoz et al. (2018) in orange, and this work in blue. Right: Plummer profile fits for Psc II, with the same assigned colors as in the middle panel.

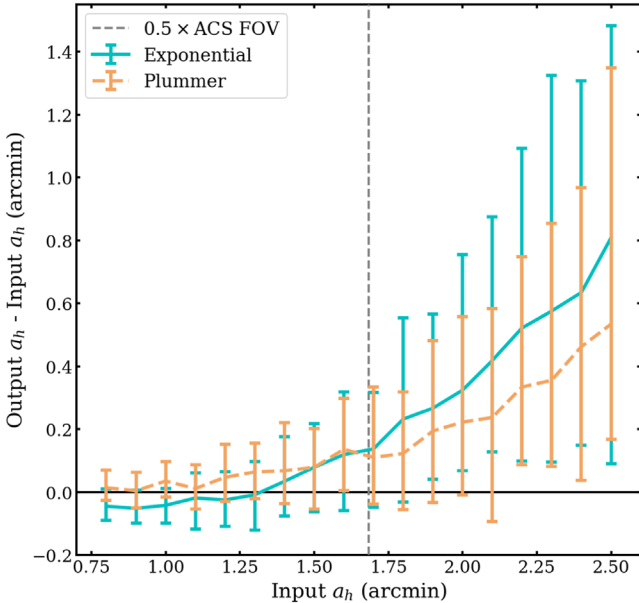


**Figure 11.** Average difference of the MCMC-fit output  $a_h$  and set input  $a_h$  for 100 mock galaxies. The exponential fit differences are shown in cyan and the Plummer profile differences in orange. The black horizontal line at 0 represents the ideal case, where the fit  $a_h$  matches the input  $a_h$ . The error bars represent the 16th and 84th percentiles from the 100 fits. The analysis for each mock galaxy is performed over an FOV equivalent to that of the HST ACS FOV, with the gray dashed vertical line marking where the input  $a_h$  begins to be greater than one-half of the ACS FOV.

of past interactions, Gaia eDR3 has provided us with the opportunity to use kinematics to study the UFDs’ possible shared history. With PMs in hand, Peg III and Psc II are among the first pairs of UFDs to be investigated further in this context.

To calculate a rough estimate of the likelihood that two satellite galaxies at similarly large distances and with radial velocities comparable to Peg III and Psc II would appear together by chance (i.e., not associated with each other prior to entering the MW halo) with a similar relative distance and

**Table 3**  
Adopted and Derived Values for Peg III and Psc II

Parameter	Peg III	Psc II
$(m - M)_0$	$21.66 \pm 0.12$	$21.31 \pm 0.17$
$v_{\text{GSR}}$ (km s $^{-1}$ )	$-67.6 \pm 2.6$	$-79.9 \pm 2.7$
$\sigma_v$ (km s $^{-1}$ )	$5.4^{+3.0}_{-2.5}$	$5.4^{+3.6}_{-2.4}$
$\mu_\alpha \cos \delta$ (mas yr $^{-1}$ )	$0.06 \pm 0.1$	$0.11 \pm 0.11$
$\mu_\delta$ (mas yr $^{-1}$ )	$-0.2 \pm 0.1$	$-0.24^{+0.12}_{-0.11}$
$r_h$ (arcmin)	$1.51^{+0.35}_{-0.29}$	$1.04 \pm 0.08$
$r_h$ (pc)	$94^{+25}_{-24}$	$55 \pm 6$
$m_V$	$17.50^{+0.15}_{-0.21}$	$17.03 \pm 0.04$
$M_{1/2}$ ( $10^6 M_\odot$ )	$3.2^{+4.3}_{-2.1}$	$1.9^{+3.3}_{-1.3}$
$(M/L_V)_{1/2}$ ( $M_\odot / L_\odot$ )	$1600^{+480}_{-580}$	$850^{+570}_{-260}$

**Note.** The Peg III distance modulus is from Kim et al. (2016), and the distance modulus for Psc II is from Sand et al. (2012). The  $\sigma_v$  values are from Kim et al. (2016) and Kirby et al. (2015) for Peg III and Psc II, respectively, while the PMs are both taken from McConnachie & Venn (2020). The azimuthally averaged half-light radius  $r_h$  is calculated using the relation  $r_h = a_h \sqrt{1 - \epsilon}$ .  $(M/L_V)_{1/2}$  is the mass-to-light ratio within the elliptical half-light radius. The processes for the derivation of  $m_V$ ,  $M_{1/2}$ , and  $(M/L_V)_{1/2}$  are described in Sections 3.3 and 3.4. The uncertainties on all derived quantities are the 16th and 84th percentiles of MC simulations including the full-error space of all the relevant terms.

radial velocity difference between them, we drew  $10^6$  UFDs from a Gaussian velocity distribution centered around  $0 \text{ km s}^{-1}$  with  $\sigma = 100 \text{ km s}^{-1}$  and a distance distribution of  $r^{3-1-\gamma}$  from  $30\text{--}300 \text{ kpc}$ , with  $\gamma = 2.11$  taken from Fritz et al. (2020). We compared the drawn distance and velocity values to those of Psc II, calculating the percentage of these UFDs with  $\Delta v \leq 15 \text{ km s}^{-1}$  and  $\Delta r \leq 40 \text{ kpc}$  with respect to the properties of Psc II ( $\sim -80 \text{ km s}^{-1}$ ;  $\sim 183 \text{ kpc}$ ). Of the  $10^6$  draws, 2.5% met the criteria, suggesting a low probability that two galaxies with such similar properties to each other as Peg III and Psc II share would exist in the MW halo by chance.

**Table 4**  
Orbital Parameters for Peg III and Psc II Using the McConnachie & Venn (2020) PMs for Both Galaxies

Orbit	MW-only Potential					
	$f_{\text{peri}}$	$t_{\text{peri}}$ [Gyr]	$r_{\text{peri}}$ [kpc]	$f_{\text{apo}}$	$t_{\text{apo}}$ [Gyr]	$r_{\text{apo}}$ [kpc]
MW1						
PegIII-MW	0.53	2.56 [2.61,4.53]	20 [24,115]	0.67	0.58 [0.64,2.61]	217 [205,279]
PscII-MW	0.58	2.56 [2.54,4.65]	9 [22,103]	0.70	0.71 [0.71,2.42]	203 [196,270]
PegIII-PscII	0.75	1.8 [0.06,3.65]	12 [20,113]	0.61	2.4 [2.21,4.63]	17 [159,572]
MW2						
PegIII-MW	0.7	2.07 [2.14,4.12]	15 [26,130]	0.82	0.42 [0.46,2.24]	213 [201,278]
PscII-MW	0.73	2.06 [2.05,3.85]	11 [22,112]	0.84	0.5 [0.51,2.23]	197 [189,269]
PegIII-PscII	0.84	2.1 [0.07,3.47]	7 [22,128]	0.82	5.31 [1.8,4.05]	256 [146,523]

**Note.** The orbital parameters listed here are for the representative cases shown in Figure 12, rather than the median orbital history. The listed uncertainties correspond to the 16th and 84th percentiles around the median of the distributions calculated using 1000 MC samples in the MW-only potential to illustrate the range of orbital uncertainty.  $f_{\text{peri}}$  ( $f_{\text{apo}}$ ) is the fraction of 1000 orbits where a pericenter (apocenter) is recovered,  $t_{\text{peri}}$  ( $t_{\text{apo}}$ ) is the time at which the pericenter (apocenter) occurs on average, and  $r_{\text{peri}}$  ( $r_{\text{apo}}$ ) is the distance of the most recent pericenter (apocenter). Pericenter and apocenter are defined as the critical minima and maxima along orbital trajectories in Galactocentric distance.

Furthermore, we can use the orbital histories computed using the McConnachie & Venn (2020) PMs to speculate about whether Peg III and Psc II have a shared orbital history or one that indicates that they have been bound in the recent past. The bottom panel of Figure 12 shows the orbits of Peg III and Psc II with respect to one another in the MW-only (dashed lines) and MW-LMC potential (solid lines). In the MW-only potential, the satellites reach as close 20 kpc to each other in the last 2–3 Gyr. For the heavy MW-only potential, Peg III and Psc II remain significantly far from each other until  $\sim 2$  Gyr ago, when they make a close ( $< 20$  kpc), pericentric passage about both the MW and then subsequently each other. However, for the light MW-only potential, the UFDs have remained within 80 kpc of each other for at least the last few billion years.

When the influence of the LMC is included, an opposite trend is observed. For the light MW model, the UFDs first interact with one another about 3 Gyr ago (prior to the infall of the LMC) and then pass about each other again 1 Gyr ago (after the infall of the LMC). They are otherwise significantly separated. In the heavy MW+LMC model, the UFDs are within about 80 kpc of each other for the last 6 Gyr. They pass around each other twice at a distance of  $\sim 20$  kpc at  $\sim 1$  and  $\sim 2$  Gyr ago. These results, summarized in Tables 4 and 5, illustrate that Peg III and Psc II may have had an intricate orbital history that includes close interactions with the MW, LMC, and each other when the McConnachie & Venn (2020) values are considered. These conclusions are based on the direct orbital histories, yet the results in Tables 4 and 5 illustrate that there is significant statistical uncertainty on the properties of this system due to large measurement uncertainties on distance and PM.

We also calculate a simple metric to test whether Peg III and Psc II are currently bound to each other as was done in Geha et al. (2015) and Sohn et al. (2020) for NGC 147 and NGC 185, two dwarf elliptical galaxies located about  $1^\circ$  from each other. It is known that for two point masses to be gravitationally bound, the potential energy of the system must be greater than the kinetic energy. This yields the criterion  $b \equiv 2GM_{\text{sys}}/\Delta r\Delta v^2$ . Thus, when  $b > 1$ , the system is considered bound.

Assuming a relative Galactocentric distance of  $\Delta r = 36.4$  kpc between the dwarfs, a relative Galactocentric velocity of  $\Delta v = 20.6$  km s $^{-1}$  at present day, and a mass of

$10^9 M_\odot$  for each dwarf, we find  $b = 1.11 \pm 0.31$ . This  $b$  corresponds to the initial conditions used to calculate the direct orbital histories, and the uncertainty represents the standard deviation across  $b$  calculated for 1000 initial conditions encompassing the measured phase space of these two dwarf galaxies. Thus, Peg III and Psc II are consistent with being bound to each other, as illustrated by the orbital histories in the bottom panels of Figure 12. However, the uncertainty on  $b$  indicates that some unbound orbits are possible within the measured phase space. This, in combination with the nonzero transverse motions of these dwarfs, indicates that improved distances and PMs, in addition to a more precise understanding of the MW’s mass, are therefore necessary to definitively conclude whether Peg III and Psc II have experienced a shared orbital history over the last few billion years.

If Peg III and Psc II are indeed bound to each other, as suggested by the most common orbits recovered from the McConnachie & Venn (2020) PMs, this would add to the rare findings of confirmed pairs of satellites within the Local Group. It has also been shown that pairs and groups of satellites that fall into the halo of their hosts together tend to merge with one another, sometimes only 1–3 Gyr after infall (e.g., Deason et al. 2014; Wetzel et al. 2015). Peg III and Psc II could thus be in the process of or on the way to the early phases of merging. Conversely, another possibility would be for the two UFDs to disperse in phase space soon after falling into the MW, depending on how strongly the two were bound during infall (e.g., Deason et al. 2015). Improved PMs will continue to shed light on the potential future trajectories of these UFDs.

### 5.3. Need for Improved PM Measurements

Based on Gaia eDR3 measurements alone, it is unlikely for the possibility of an association between Peg III and Psc II to be further constrained. Gaia will operate much longer, however, optimistically achieving a baseline of 11 yr. Since PM errors of continuously observing telescopes scale with time to the power of  $-1.5$  (e.g., Lindegren et al. 2021), the precision achievable with the final Gaia data release would be approximately 36 and 30 km s $^{-1}$  for Peg III and Psc II, respectively. This precision could already be met and surpassed using HST now. We estimate the achievable precision using the data described here



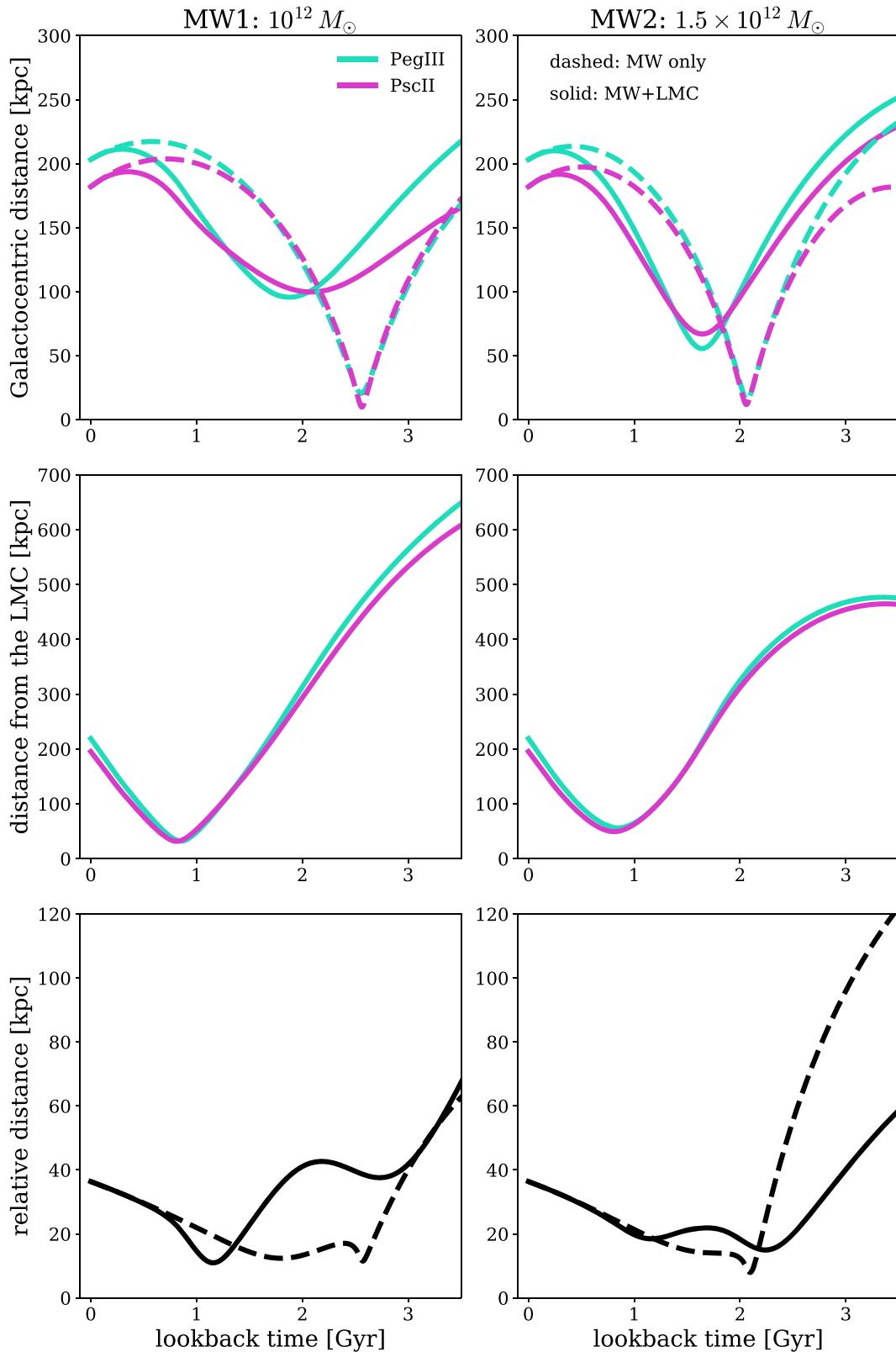


**Figure 12.** Top: direct orbital histories of Peg III (cyan) and Psc II (magenta) relative to the MW, the LMC, and to each other are shown in the top, middle, and bottom panels, respectively. Gaia eDR3 PMs from McConnachie & Venn (2020) are used for both Peg III and Psc II. MW1 (left) has a virial mass of  $10^{12} M_{\odot}$  while MW2 (right) has a virial mass of  $1.5 \times 10^{12} M_{\odot}$ . Dashed lines represent orbits computed in an MW-only potential and solid lines indicate an MW+LMC potential with an LMC mass of  $1.8 \times 10^{11} M_{\odot}$ . The presence of the LMC decreases the distance at the pericenter relative to the MW-only model by  $\sim 40\text{--}80$  kpc. Middle: the orbital history of each UFD relative to the LMC. For both MW1 and MW2, the satellites complete a pericentric passage about the LMC at  $\sim 1$  Gyr ago. Bottom: the orbit of Peg III and Psc II relative to one another. In both MW potentials, when the LMC is included, the two UFDs remained within  $\sim 60$  kpc of each other in the last 4 Gyr, indicating that the satellites may be an interacting pair that could have originated in a similar environment.

**Table 5**  
Same as Table 4, but for the MW-LMC Potential

Orbit	MW-LMC Potential					
	$f_{\text{peri}}$	$t_{\text{peri}}$ [Gyr]	$r_{\text{peri}}$ [kpc] MW1	$f_{\text{apo}}$	$t_{\text{apo}}$ [Gyr]	$r_{\text{apo}}$ [kpc]
PegIII-MW	0.71	1.88 [1.81,3.12]	95 [29,145]	0.76	0.3 [0.3,0.74]	211 [194,239]
PegIII-LMC	0.71	0.85 [1.81,3.12]	32 [29,145]	0.76	5.92 [0.3,0.74]	817 [194,239]
PscII-MW	0.72	2.08 [1.75,3.3]	99 [31,125]	0.81	0.35 [0.33,1.05]	193 [182,225]
PscII-LMC	0.72	0.81 [1.75,3.3]	31 [31,125]	0.81	4.8 [0.33,1.05]	685 [182,225]
PegIII-PscII	0.8	1.16 [0.06,2.7]	10 [21,97]	0.75	2.18 [1.4,4.05]	42 [106,441]
MW2						
PegIII-MW	0.8	1.64 [1.59,2.64]	55 [31,150]	0.89	0.25 [0.25,0.82]	210 [193,248]
PegIII-LMC	0.8	0.85 [1.59,2.64]	56 [31,150]	0.89	3.35 [0.25,0.82]	476 [193,248]
PscII-MW	0.82	1.64 [1.5,2.79]	66 [32,136]	0.91	0.29 [0.28,1.22]	191 [180,227]
PscII-LMC	0.82	0.81 [1.5,2.79]	49 [32,136]	0.91	3.38 [0.28,1.22]	464 [180,227]
PegIII-PscII	0.88	1.16 [0.07,2.84]	18 [21,113]	0.9	1.7 [1.28,3.49]	21 [109,440]

**Note.** Here, the orbital parameters of Peg III and Psc II calculated relative to the LMC's orbit are also included.

as a first epoch and with a second epoch taken as outlined in Kallivayalil et al. (2015). A new measurement with HST imaging taken in 2023 (a 6 yr baseline) would measure the transverse velocity to a precision in both dimensions of  $30.3 \text{ km s}^{-1}$  for Peg III and  $24.5 \text{ km s}^{-1}$  for Psc II. If a velocity difference less than  $\sim 50 \text{ km s}^{-1}$  was observed, we would be able to exclude the possibility of a chance association at a confidence level of at least 95% (see the Appendix for detailed calculations).

## 6. Conclusions

Based on deep HST imaging and Gaia eDR3 PMs, we have measured the structural parameters and performed an orbital analyses for two distant MW UFD satellites, Peg III and Psc II. For PegIII, we measured an elliptical half-light radius of  $1.88_{-0.33}^{+0.42}$ , a position angle of  $85^\circ \pm 8^\circ$ , and an ellipticity of  $0.36_{-0.10}^{+0.09}$ . The best-fit exponential model for Psc II gave an elliptical half-light radius of  $1.31_{-0.09}^{+0.10}$ , a position angle of  $97^\circ \pm 3^\circ$ , and an ellipticity of  $0.37 \pm 0.04$ . Our Psc II measurements are within  $1\sigma$  agreement when compared to previous literature values, while we find a larger elliptical half-light radius value for Peg III. See Tables 1 and 2 for full comparisons. Future imaging of similar depth to ours paired with a larger FOV would help clarify the true size of Peg III.

We compared the measured sizes and magnitudes of Peg III and Psc II to both those of other observed faint MW satellites and simulations of isolated field UFDs and satellite UFDs in an MW-like environment. While Peg III and Psc II are more distant MW UFDs with  $r_h$  and  $M_V$  values that correspond well to simulations of isolated field UFDs, they are not significantly distinct in structure from other observed UFDs in the inner MW halo. This could point to Peg III and Psc II (and other outer-halo UFDs) having been subject to tidal forces from the MW and/or the LMC throughout their lifetimes.

The first orbital analysis, using solely the McConnachie & Venn (2020) PM values, demonstrated the importance of including the LMC in such calculations, as it affects the timing and pericenter of the orbits of both UFDs. In this analysis, a statistically significant fraction of the computed orbital histories

in the measured phase space show Peg III and Psc II are consistent with being a gravitationally bound pair today.

Comparing the vastly different results from the Li et al. (2021) study versus our analysis using the McConnachie & Venn (2020) Psc II PM values and considering that the Peg III PM measurement came from a single star, it is also clear that improved measurements based on more member stars and a clearer knowledge of the MW's mass are necessary to narrow down the possible orbital histories and allow a more definitive statement on whether Peg III and Psc II are indeed a bound pair. These improved measurements could be taken from imaging by HST now or measured from the final Gaia data release in years to come. With the precision achievable from these baselines, measuring a velocity difference between Peg III and Psc II of less than  $\sim 50 \text{ km s}^{-1}$  would suggest with about 95% confidence that these UFDs are bound. This would finally resolve the question and confirm whether these two fascinating galaxies are indeed bound, thereby providing a critical data point for understanding dwarf galaxy evolution.

We would like to thank the anonymous referee for their thorough reading of this manuscript and comments that have led to its improvement and clarification. These data are associated with the HST Treasury Program 14734 (PI: N. Kallivayalil). Support for this program was provided by NASA through grants from the Space Telescope Science Institute. This material is based upon work supported by the National Science Foundation under grant No. AST-1847909. H.R. acknowledges support from the Virginia Space Grant Consortium Graduate Research STEM Fellowship. E.P. acknowledges support from the Miller Institute for Basic Research in Science at the University of California Berkeley. This research has made use of NASA's Astrophysics Data System.

*Facility:* HST (ACS, WFC3),

*Software:* Apy (Robitaille & Bressert 2012); Astrodizzle (Fruchter & Hook 2002); Astropy (Astropy Collaboration et al. 2013, 2018); corner.py (Foreman-Mackey 2016); dustmaps (Green 2018); emcee (Foreman-Mackey et al. 2013); Jupyter Notebook (Kluyver et al. 2016); Matplotlib (Hunter 2007); NumPy (Harris et al. 2020); photutils (Bradley et al. 2020); scikitlearn (Pedregosa et al. 2012); SciPy

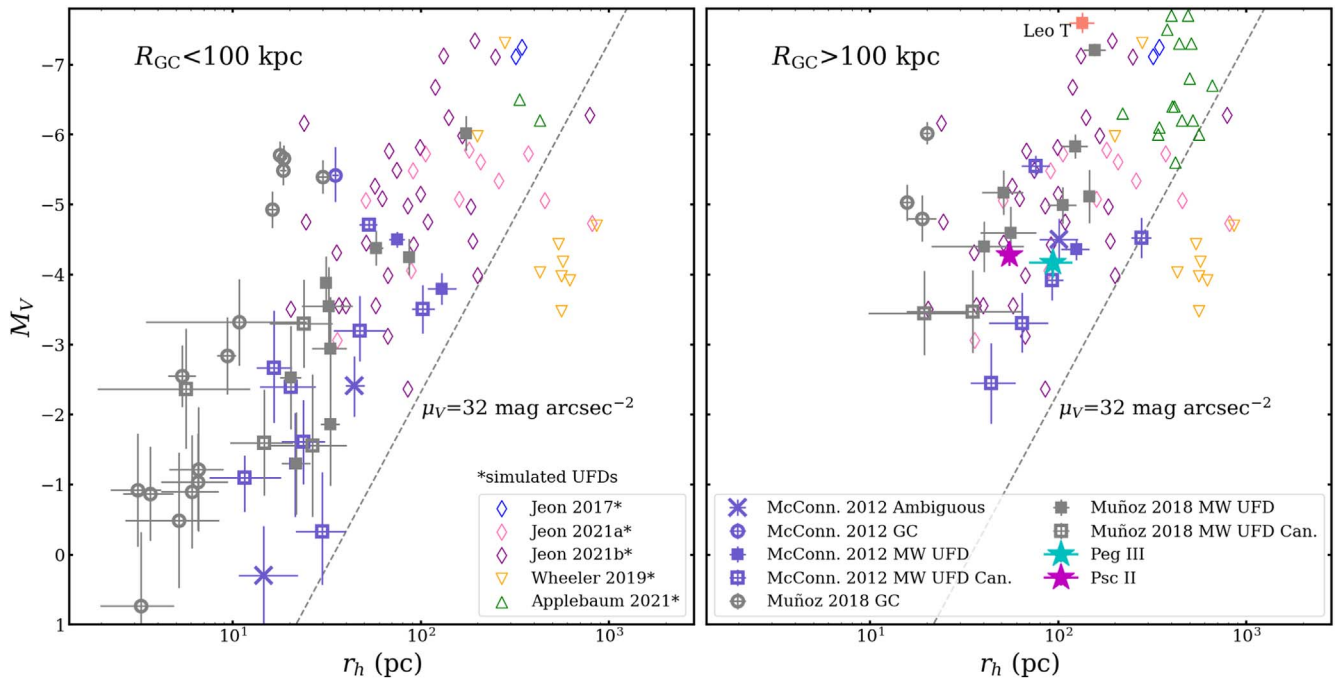


**Figure 13.** Comparison of simulated UFDs to observed MW satellites. The simulated UFDs (Jeon et al. 2017, blue diamonds; Jeon et al. 2021a, pink diamonds; Jeon et al. 2021b, purple diamonds; Wheeler et al. 2019, orange inverted triangles) are the same in both panels, except for those of Applebaum et al. (2021, green triangles), which are split between the two panels based on their simulated Galactocentric distances. Simulated UFDs can be distinguished from observed satellites as the latter all have error bars. The observed data are also split based on their Galactocentric distance, with satellites within 100 kpc shown in the left panel and satellites beyond 100 kpc in the right. Confirmed MW UFDs are shown as filled squares, candidate MW UFDs as open squares, MW globular clusters as open circles, and ambiguous MW satellites as x’s. The purple symbols use data from the updated McConnachie (2012) table, while the gray symbols (and Leo T, in orange) are from Muñoz et al. (2018). The dashed line represents a constant surface brightness of  $32 \text{ mag arcsec}^{-2}$ , approximately the current observational limit. Our measured Peg III (cyan star) and Psc II (magenta star) half-light radius and  $M_V$  values lie in the right panel, within the  $r_h$  and  $M_V$  range of other MW UFDs as well as the Jeon et al. (2021a, 2021b) simulated field UFDs. Some inner-halo satellites from the left panel also fall within the Jeon et al. (2021a, 2021b) range.

(Virtanen et al. 2020); stsynphot (STScI Development Team 2010); synphot (STScI Development Team 2018),

the velocity difference for each realization:

$$V_{\text{diff}} = \sqrt{(V_{\text{Psc II},X} - V_{\text{Peg III},X})^2 + (V_{\text{Psc II},Y} - V_{\text{Peg III},Y})^2}. \quad (\text{A1})$$

## Appendix Calculations of Current and Future Precision

To formally investigate the precision needed for determining an association, we perform an MC simulation, drawing the transverse velocities in both dimensions (X and Y) for two galaxies in both an unassociated and associated case. To do this, we must consider the dispersion of the halo ( $\sim 100 \text{ km s}^{-1}$ ; Correa Magnus & Vasiliev 2022) as well as the PM uncertainties. Gaia’s current measurement errors for the two UFDs are clearly larger than the halo dispersion: without using a prior (which artificially constrains the error), the best measurement determined for Psc II using Gaia eDR3 has a precision of about  $230 \text{ km s}^{-1}$  (Li et al. 2021), while a PM uncertainty cannot even be obtained for Peg III. Nonetheless, to calculate an estimate of the necessary precision for determining the presence of an association, we optimistically scale the Li et al. (2021) PM error by the Kim et al. (2016) distance to obtain  $270 \text{ km s}^{-1}$  for Peg III.

In the unassociated case, transverse velocities for two galaxies are drawn from a Gaussian distribution centered on  $0 \text{ km s}^{-1}$ , with  $1\sigma$  equal to the halo dispersion of  $100 \text{ km s}^{-1}$  plus the measurement errors of each galaxy, as described in the previous paragraph.

In the associated case, we again center the Gaussian distribution on  $0 \text{ km s}^{-1}$ , but instead set  $1\sigma$  equal to only the current Gaia eDR3 measurement errors of Peg III and Psc II (i.e., without including the halo dispersion). We then calculate

We take the median  $V_{\text{diff}}$  from the associated case and compare it to the  $V_{\text{diff}}$  values calculated in the unassociated case and determine how often the unassociated case produces a velocity difference less than or equal to the median associated  $V_{\text{diff}}$ . We obtain a median  $V_{\text{diff}} = 418 \text{ km s}^{-1}$  from the associated realizations. A velocity difference of this size or smaller occurs with a 45% probability in the unassociated case. Thus, it is not expected that Gaia eDR3 measurements without a prior could give any constraints on whether or not Peg III and Psc II are associated.

Now we investigate how future measurements could improve upon current information to constrain an association between Peg III and Psc II.












Repeating the MC simulation with the estimated HST errors from a 6 yr baseline (Peg III:  $30.3 \text{ km s}^{-1}$ ; Psc II:  $24.5 \text{ km s}^{-1}$ ), we obtain a median  $V_{\text{diff}} = 46 \text{ km s}^{-1}$  from the associated cases. A velocity difference of this size or smaller occurs with a 4.7% probability in the unassociated case. Thus, for an observed velocity difference of less than  $\sim 50 \text{ km s}^{-1}$ , the small probability from the unassociated MC cases, combined with the already small probability of similar LOS velocities and distances (2.5%, see Section 5.2), would almost completely rule out a chance association.

Given a longer baseline, HST(-like) observations taken with HST, the James Webb Space Telescope, or the Roman Space Telescope could measure the velocity well enough to prove that the two systems are associated with each other. For example,



observations taken in 2034 would give a full transverse velocity error of  $19.4 \text{ km s}^{-1}$ , smaller than the current Galactocentric velocity difference ( $\sim 20.6 \text{ km s}^{-1}$ ).

### ORCID iDs

Hannah Richstein  <https://orcid.org/0000-0002-3188-2718>  
 Ekta Patel  <https://orcid.org/0000-0002-9820-1219>  
 Nitya Kallivayalil  <https://orcid.org/0000-0002-3204-1742>  
 Joshua D. Simon  <https://orcid.org/0000-0002-4733-4994>  
 Paul Zivick  <https://orcid.org/0000-0001-9409-3911>  
 Erik Tollerud  <https://orcid.org/0000-0002-9599-310X>  
 Jack T. Warfield  <https://orcid.org/0000-0003-1634-4644>  
 Gurtina Besla  <https://orcid.org/0000-0003-0715-2173>  
 Roeland P. van der Marel  <https://orcid.org/0000-0001-7827-7825>  
 Andrew Wetzel  <https://orcid.org/0000-0003-0603-8942>  
 Yumi Choi  <https://orcid.org/0000-0003-1680-1884>  
 Alis Deason  <https://orcid.org/0000-0001-6146-2645>  
 Marla Geha  <https://orcid.org/0000-0002-7007-9725>  
 Puragra Guhathakurta  <https://orcid.org/0000-0001-8867-4234>  
 Evan N. Kirby  <https://orcid.org/0000-0001-6196-5162>  
 Mattia Libralato  <https://orcid.org/0000-0001-9673-7397>  
 Elena Sacchi  <https://orcid.org/0000-0001-5618-0109>  
 Sangmo Tony Sohn  <https://orcid.org/0000-0001-8368-0221>

### References

- Ahn, C. P., Alexandroff, R., Allende Prieto, C., et al. 2014, *ApJS*, 211, 17  
 Applebaum, E., Brooks, A. M., Christensen, C. R., et al. 2021, *ApJ*, 906, 96  
 Astropy Collaboration, Price-Whelan, A. M., Sipőcz, B. M., et al. 2018, *AJ*, 156, 123  
 Astropy Collaboration, Robitaille, T. P., Tollerud, E. J., et al. 2013, *A&A*, 558, A33  
 Battaglia, G., Taibi, S., Thomas, G. F., & Fritz, T. K. 2022, *A&A*, 657, A54  
 Belokurov, V., Walker, M. G., Evans, N. W., et al. 2010, *ApJL*, 712, L103  
 Besla, G., Hernquist, L., & Loeb, A. 2013, *MNRAS*, 428, 2342  
 Besla, G., Kallivayalil, N., Hernquist, L., et al. 2012, *MNRAS*, 421, 2109  
 Besla, G., Martínez-Delgado, D., van der Marel, R. P., et al. 2016, *ApJ*, 825, 20  
 Bovill, M. S., & Ricotti, M. 2009, *ApJ*, 693, 1859  
 Bradley, L., Sipőcz, B., Robitaille, T., et al. 2020, *astropy/photutils*: 1.0.0, Zenodo, doi:10.5281/zenodo.4044744  
 Breddels, M. A., & Helmi, A. 2013, *A&A*, 558, A35  
 Bressan, A., Fagotto, F., Bertelli, G., & Chiosi, C. 1993, *A&AS*, 100, 647  
 Bullock, J. S., & Boylan-Kolchin, M. 2017, *ARA&A*, 55, 343  
 Caldwell, N., Walker, M. G., Mateo, M., et al. 2017, *ApJ*, 839, 20  
 Correa Magnus, L., & Vasiliev, E. 2022, *MNRAS*, 511, 2610  
 Deason, A., Wetzel, A., & Garrison-Kimmel, S. 2014, *ApJ*, 794, 115  
 Deason, A. J., Wetzel, A. R., Garrison-Kimmel, S., & Belokurov, V. 2015, *MNRAS*, 453, 3568  
 Drlica-Wagner, A., Bechtol, K., Mau, S., et al. 2020, *ApJ*, 893, 47  
 D'Souza, R., & Bell, E. F. 2022, *MNRAS*, 512, 739  
 Errani, R., Peñarrubia, J., & Walker, M. G. 2018, *MNRAS*, 481, 5073  
 Fagotto, F., Bressan, A., Bertelli, G., & Chiosi, C. 1994a, *A&AS*, 104, 365  
 Fagotto, F., Bressan, A., Bertelli, G., & Chiosi, C. 1994b, *A&AS*, 105, 29  
 Flores, R. A., & Primack, J. R. 1994, *ApJL*, 427, L1  
 Foreman-Mackey, D. 2016, *JOSS*, 1, 24  
 Foreman-Mackey, D., Hogg, D. W., Lang, D., & Goodman, J. 2013, *PASP*, 125, 306  
 Fritz, T. K., Battaglia, G., Pawlowski, M. S., et al. 2018, *A&A*, 619, A103  
 Fritz, T. K., Di Cintio, A., Battaglia, G., Brook, C., & Taibi, S. 2020, *MNRAS*, 494, 5178  
 Fruchter, A. S., & Hook, R. N. 2002, *PASP*, 114, 144  
 Gaia Collaboration, Brown, A. G. A., Vallenari, A., et al. 2021, *A&A*, 649, A1  
 Fu, S. W., Simon, J. D., & Alarcón Jara, A. G. 2019, *ApJ*, 883, 11  
 Gaia Collaboration, Prusti, T., & de Bruijne, J. H. J. 2016, *A&A*, 595, A1  
 Garavito-Camargo, N., Besla, G., Laporte, C. F. P., et al. 2019, *ApJ*, 884, 51  
 Garavito-Camargo, N., Besla, G., Laporte, C. F. P., et al. 2021, *ApJ*, 919, 109  
 Garofalo, A., Tantaló, M., Cusano, F., et al. 2021, *ApJ*, 916, 10  
 Geha, M., Weisz, D., Grocholski, A., et al. 2015, *ApJ*, 811, 114  
 Girardi, L., Bressan, A., Bertelli, G., & Chiosi, C. 2000, *A&AS*, 141, 371  
 Gnedin, N. Y., & Kravtsov, A. V. 2006, *ApJ*, 645, 1054  
 Goerdt, T., Moore, B., Read, J. I., Stadel, J., & Zemp, M. 2006, *MNRAS*, 368, 1073  
 Grand, R. J. J., Marinacci, F., Pakmor, R., et al. 2021, *MNRAS*, 507, 4953  
 Green, G. 2018, *JOSS*, 3, 695  
 Guerra, J., Geha, M., & Strigari, L. E. 2021, arXiv:2112.05166  
 Guo, Q., White, S., Boylan-Kolchin, M., et al. 2011, *MNRAS*, 413, 101  
 Harris, C. R., Millman, K. J., van der Walt, S. J., et al. 2020, *Natur*, 585, 357  
 Hunter, J. D. 2007, *CSE*, 9, 90  
 Jardel, J. R., & Gebhardt, K. 2013, *ApJL*, 775, L30  
 Jeon, M., Besla, G., & Bromm, V. 2017, *ApJ*, 848, 85  
 Jeon, M., Besla, G., & Bromm, V. 2021a, *MNRAS*, 506, 1850  
 Jeon, M., Bromm, V., Besla, G., Yoon, J., & Choi, Y. 2021b, *MNRAS*, 502, 1  
 Ji, A. P., Koposov, S. E., Li, T. S., et al. 2021, *ApJ*, 921, 32  
 Kallivayalil, N., Wetzel, A. R., Simon, J. D., et al. 2015, arXiv:1503.01785  
 Kim, D., Jerjen, H., Geha, M., et al. 2016, *ApJ*, 833, 16  
 Kim, D., Jerjen, H., Mackey, D., Da Costa, G. S., & Milone, A. P. 2015, *ApJL*, 804, L44  
 Kim, S., Staveley-Smith, L., Dopita, M. A., et al. 1998, *ApJ*, 503, 674  
 Kirby, E. N., Simon, J. D., & Cohen, J. G. 2015, *ApJ*, 810, 56  
 Kluyver, T., Ragan-Kelley, B., Pérez, F., et al. 2016, in *Positioning and Power in Academic Publishing: Players, Agents and Agendas*, ed. F. Loizides & B. Schmidt (Amsterdam: IOS Press), 87  
 Leitherer, C., Schaerer, D., Goldader, J. D., et al. 1999, *ApJS*, 123, 3  
 Li, H., Hammer, F., Babusiaux, C., et al. 2021, *ApJ*, 916, 8  
 Lindegren, L., Klioner, S. A., Hernández, J., et al. 2021, *A&A*, 649, A2  
 Mackey, A. D., Koposov, S. E., Erkal, D., et al. 2016, *MNRAS*, 459, 239  
 Majewski, S. R., Nidever, D. L., Muñoz, R. R., et al. 2009, in *IAU Symp. 256, The Magellanic System: Stars, Gas, and Galaxies*, ed. J. T. Van Loon & J. M. Oliveira (Cambridge: Cambridge Univ. Press), 51  
 Martin, N. F., de Jong, J. T. A., & Rix, H.-W. 2008, *ApJ*, 684, 1075  
 McConnachie, A. W. 2012, *AJ*, 144, 4  
 McConnachie, A. W., & Venn, K. A. 2020, *RNAAS*, 4, 229  
 Moore, B. 1994, *Natur*, 370, 629  
 Muñoz, R. R., Côté, P., Santana, F. A., et al. 2018, *ApJ*, 860, 66  
 Muñoz, R. R., Padmanabhan, N., & Geha, M. 2012, *ApJ*, 745, 127  
 Navarro, J. F., Frenk, C. S., & White, S. D. M. 1997, *ApJ*, 490, 493  
 Pace, A. B., Erkal, D., & Li, T. S. 2022, arXiv:2205.05699  
 Patel, E., Besla, G., & Sohn, S. T. 2017, *MNRAS*, 464, 3825  
 Patel, E., Kallivayalil, N., Garavito-Camargo, N., et al. 2020, *ApJ*, 893, 121  
 Pawlowski, M. S. 2021, *Galax*, 9, 66  
 Pedregosa, F., Varoquaux, G., Gramfort, A., et al. 2012, arXiv:1201.0490  
 Plummer, H. C. 1911, *MNRAS*, 71, 460  
 Read, J. I., & Gilmore, G. 2005, *MNRAS*, 356, 107  
 Read, J. I., Mamon, G. A., Vasiliev, E., et al. 2021, *MNRAS*, 501, 978  
 Read, J. I., Walker, M. G., & Steger, P. 2018, *MNRAS*, 481, 860  
 Read, J. I., Walker, M. G., & Steger, P. 2019, *MNRAS*, 484, 1401  
 Ricotti, M., & Gnedin, N. Y. 2005, *ApJ*, 629, 259  
 Robitaille, T., & Bressert, E. 2012, *APLpy: Astronomical Plotting Library in Python*, Astrophysics Source Code Library, record ascl:1208.017  
 Saha, A., Olszewski, E. W., Brondel, B., et al. 2010, *AJ*, 140, 1719  
 Sand, D. J., Strader, J., Willman, B., et al. 2012, *ApJ*, 756, 79  
 Schlafly, E. F., & Finkbeiner, D. P. 2011, *ApJ*, 737, 103  
 Schlegel, D. J., Finkbeiner, D. P., & Davis, M. 1998, *ApJ*, 500, 525  
 Simon, J. D. 2019, *ARA&A*, 57, 375  
 Simon, J. D., Brown, T. M., Drlica-Wagner, A., et al. 2021, *ApJ*, 908, 18  
 Sirianni, M., Jee, M. J., Benítez, N., et al. 2005, *PASP*, 117, 1049  
 Skrutskie, M. F., Cutri, R. M., Stiening, R., et al. 2006, *AJ*, 131, 1163  
 Sohn, S. T., Patel, E., Fardal, M. A., et al. 2020, *ApJ*, 901, 43  
 Strigari, L. E., Bullock, J. S., Kaplinghat, M., et al. 2007, *ApJ*, 669, 676  
 Strigari, L. E., Bullock, J. S., Kaplinghat, M., et al. 2008, *Natur*, 454, 1096  
 Strigari, L. E., Frenk, C. S., & White, S. D. M. 2017, *ApJ*, 838, 123  
 STScI Development Team 2010, *stsynphot: synphot for HST and JWST*, Astrophysics Source Code Library, ascl:2010.003  
 STScI Development Team 2018, *synphot: Synthetic photometry using Astropy*, Astrophysics Source Code Library, ascl:1811.001  
 Torrealba, G., Koposov, S. E., Belokurov, V., & Irwin, M. 2016, *MNRAS*, 459, 2370  
 van der Marel, R. P., & Kallivayalil, N. 2014, *ApJ*, 781, 121  
 Virtanen, P., Gommers, R., Oliphant, T. E., et al. 2020, *NatMe*, 17, 261  
 Wetzel, A. R., Deason, A. J., & Garrison-Kimmel, S. 2015, *ApJ*, 807, 49  
 Wheeler, C., Hopkins, P. F., Pace, A. B., et al. 2019, *MNRAS*, 490, 4447  
 Willman, B., Dalcanton, J. J., Martínez-Delgado, D., et al. 2005, *ApJL*, 626, L85  
 Wolf, J., Martinez, G. D., Bullock, J. S., et al. 2010, *MNRAS*, 406, 1220  
 York, D. G., Adelman, J., Anderson, J. E. J., et al. 2000, *AJ*, 120, 1579